PHYSICAL REVIEW D **87,** 075015 (2013)

Illuminating dark matter at the ILC

Herbert K. Dreiner[*]
Physikalisches Institut and Bethe Center for Theoretical Physics, University of Bonn, Bonn D-53115, Germany

Moritz Huck[†] and Michael Krämer[‡]
Institute for Theoretical Particle Physics and Cosmology, RWTH Aachen University, Aachen D-52056, Germany

Daniel Schmeier[§] and Jamie Tattersall[‖]
Physikalisches Institut and Bethe Center for Theoretical Physics, University of Bonn, Bonn D-53115, Germany
(Received 14 December 2012; published 19 April 2013)

The weakly interacting massive particle paradigm for dark matter is currently being probed via many different experiments. Direct detection, indirect detection and collider searches are all hoping to catch a glimpse of these elusive particles. Here, we examine the potential of the International Linear Collider (ILC) to shed light on the origin of dark matter. By using an effective field theory approach we are also able to compare the reach of the ILC with that of the other searches. We find that for low mass dark matter (< 10 GeV), the ILC offers a unique opportunity to search for interacting massive particles beyond any other experiment. In addition, if dark matter happens to only couple to leptons or via a spin dependent interaction, the ILC can give an unrivalled window to these models. We improve on previous ILC studies by constructing a comprehensive list of effective theories that allows us to move beyond the nonrelativistic approximation.

DOI: 10.1103/PhysRevD.87.075015 PACS numbers: 95.35.+d, 12.60.−i, 13.88.+e, 13.85.Rm

I. INTRODUCTION

Weakly interacting massive particles (WIMPs) are one of the leading candidates to solve the dark matter puzzle [1]. Primarily this is due to the fact that a neutral particle that interacts with roughly the strength of the weak force naturally gives the correct relic abundance. In addition many theoretical models predict that the masses of these states should exist around the scale of electroweak symmetry breaking, e.g., supersymmetry (SUSY) [2,3], universal extra dimensions (UED) [4], Little Higgs [5,6] etc.

Currently, this WIMP paradigm is being actively explored in a number of different ways. Perhaps the most well known are the direct detection searches that aim to observe interactions between the dark matter and an atomic nucleus [7]. As these are extremely low rate experiments, the detectors are typically placed deep underground to reduce background. The annihilation of dark matter into standard model particles in high density regions of our universe offers another potential method to see a signal, e.g., Ref. [8].

In particle colliders here on Earth the same interactions may be probed in the production of dark matter. Unfortunately, the fact that WIMPs are neutral and only weakly interacting means that they cannot be detected directly in these experiments. Therefore collider based searches must rely on particles produced in combination with the dark matter candidates. If dark matter is produced directly, one possibility is to use initial state radiation (ISR), such as gluon jets, or photons, that will recoil against the WIMPs.

This idea was first explored in a model independent approach for the International Linear Collider (ILC) using monophotons in a nonrelativistic approximation [9,10]. Later, detailed detector studies have been performed to understand the full capabilities of the ILC for such a signature [11–15]. Furthermore the same signature has been considered in the case of SUSY [16,17]. At the LHC (Large Hadron Collider) and Tevatron similar signals have also been studied but with a monojet signal [18–30]. All of these papers used the idea of parametrizing the dark matter interactions in the form of effective operators. This has the advantage that the bounds can be compared with those coming from direct detection and also that a nonrelativistic approximation is not required to compare with the relic density measurement. These methods have now been used by the LHC experiments to set bounds on different effective operators that are competitive with other methods [31,32]. In addition, LEP (Large Electron-Positron Collider) data has been reinterpreted to determine corresponding constraints [33].

In this paper we take the effective field theory approach to dark matter and apply this to an ILC search [34–36]. To apply the effective field theory in a consistent way we assume that the dark matter particles can only interact

[*]dreiner@th.physik.uni-bonn.de
[†]mhuck@physik.rwth-aachen.de
[‡]mkraemer@physik.rwth-aachen.de
[§]daschm@th.physik.uni-bonn.de
[‖]jamie@th.physik.uni-bonn.de

with the standard model fields via a heavy mediator. The mediator is always assumed to be too heavy to be produced directly at the ILC and thus can be integrated out. For our model choices we consider the possibility that the dark matter candidate could be a scalar, a Dirac (or Majorana) fermion or a vector particle. The same choices are taken for the heavy mediator and all combinations are considered. The collider phenomenology can vary significantly, depending on whether the mediator is exchanged in the s- or t-channel and consequently we examine both. In addition, we also study the different ways in which the mediator can couple to both the dark matter and standard model particles. We note that using the effective field theory approach allows us to move away from the nonrelativistic approximation that had previously been used in ILC studies. This can be especially important if the dark matter candidate happens to be light.[1]

For all models we compare the reach of the ILC with the bounds derived from direct and indirect detection. We also calculate the couplings expected to lead to the correct relic density and see whether the ILC can probe these regions of parameter space. We also note that an ILC search is complementary to that at the LHC thanks to the different initial state.

The paper is laid out as follows. We begin in Sec. II by explaining how we derive the effective field theories for the dark matter interactions and we explicitly give the Lagrangian for both the full and effective theory. We also describe the benchmark models that we use throughout the study. In Sec. III we describe the various astrophysical constraints on our effective theories. We begin with the calculation of the relic density abundance before moving on to explain the bounds from direct and indirect detection.

Section IV describes in detail the potential search for dark matter at the ILC. Here we explain the calculation of the signal rate and the dominant backgrounds that were considered. In addition we detail how the ILC detectors are modeled to account for relevant experimental effects. We find that the polarization of incoming beams is particularly important for many models of dark matter to discriminate the signal and background. We also investigate the advantage of a doubling of the ILC energy to $\sqrt{s} = 1$ TeV.

In Sec. V we present the results of the paper. We begin by examining the potential bounds of the ILC on the effective coupling of the dark matter model at the collider. Afterwards, we combine these results with those from direct and indirect detection to understand for which models and mass ranges the ILC presents a unique opportunity to discover dark matter. Finally in Sec. VI we conclude and summarize the main results of our work.

[1]The mass determination of a light neutralino dark matter candidate at the ILC has been discussed in Ref. [37].

II. MODELS

A. General motivation

The idea of parametrizing the interaction of a dark matter particle with standard model particles by using effective operators is not new, see for example Refs. [19,33,35,36,38,39]. Many authors construct a list of effective 4-particle-interactions with Lorentz-invariant combinations of γ^μ, ∂_μ and spinor-/vector-indices up to mass dimension 5 or 6. In many cases there is no explanation how those operators may arise in an underlying fundamental theory. That makes it difficult to judge how exhaustive the lists of operators are, whether interference between different operators should be taken into account and how the effective model is connected to realistic fundamental theories and their couplings.

We follow the effective approach introduced in Ref. [36] by starting from different fundamental theories with given renormalizable interactions between standard model fermions and the hypothesized dark matter particles that are mediated by a very massive particle. In general we assume that the dark matter particle is colorless, an SU(2) singlet and carries no hypercharge. However, we also mention possible models where the dark matter candidate may be charged under SU(2).

From these theories we deduce effective 4-particle-vertices for energies significantly smaller than the mass of the mediator. Working with these effective operators, one can deduce information about the effective coupling and propagate this information to the parameters of the corresponding underlying fundamental theory. The effective approach allows us to reduce the dimensionality of the parameter space and more easily compare the different experimental searches.

B. Deriving effective Lagrangians

We start with a list of fundamental Lagrangians taken from Ref. [36]. However we do not perform a nonrelativistic approximation, since we are interested in the phenomenology of this Lagrangian at a high energy experiment and therefore the results for our effective operators differ. We also use a different method to evaluate the effective vertices, motivated in Ref. [40], which uses the path integral formalism.

We give one explicit example for the derivation of the effective operators and only mention specific peculiarities for the other cases, which are apart from that calculated similarly. Let ψ be a standard model fermion and χ a complex scalar field representing the dark matter candidate. For our example, we assume the mediator to be a real vector field, Z^μ, with mass M_Ω (we will keep this notation for the mediator mass throughout). We further assume that the vector particle couples only to left-chiral fermions. The relevant terms in the UV completed Lagrangian are then given by

$$\mathcal{L}_{\rm UV} = \frac{1}{2}M_\Omega^2 Z^\mu Z_\mu - \frac{1}{4}(\partial^\mu Z^\nu - \partial^\nu Z^\mu)(\partial_\mu Z_\nu - \partial_\nu Z_\mu) + g_\chi(\chi^\dagger \partial^\mu \chi + \chi \partial^\mu \chi^\dagger)V_\mu - g_l \bar{\psi}\gamma^\mu P_L \psi V_\mu, \quad (1)$$

$$\equiv \frac{1}{2}Z^\mu[(\Box - M_\Omega^2)g_{\mu\nu} - \partial_\mu\partial_\nu]Z^\nu + F^\mu Z_\mu, \quad (2)$$

where the function F^μ is given by

$$F^\mu \equiv g_\chi(\chi^\dagger \partial^\mu \chi - \chi \partial^\mu \chi^\dagger) + g_l \bar{\psi}\gamma^\mu P_L \psi. \quad (3)$$

We have not included the kinetic terms for χ, ψ, as they are not relevant for the computation of the effective Lagrangian. In this particular example, g_l and g_χ are dimensionless couplings whose definitions can change depending upon the precise model studied and we shall use this notation throughout. We have included the kinetic term for Z^μ, the heavy mediator field. After integrating it out we obtain the effective Lagrangian,

$$\mathcal{L}_{\rm eff} = \frac{1}{2M_\Omega^2}F^\mu F_\mu \quad (4)$$

$$\supset \frac{g_\chi g_l}{M_\Omega^2}\bar{\psi}\gamma^\mu P_L \psi(\chi^\dagger \partial_\mu \chi - \chi \partial_\mu \chi^\dagger). \quad (5)$$

Cases with different spin for the dark matter or the mediator particle are evaluated similarly. The full list of models with their respective fundamental and effective Lagrangians is given in Table I. We only want to give some special remarks:

(i) For spin-1/2 mediators, the Dirac propagator has only one power of M_Ω in the denominator,

$$\frac{1}{\not{p} - M_\Omega} \approx -\frac{1}{M_\Omega} - \frac{\not{p}}{M_\Omega^2}. \quad (6)$$

We therefore get two effective vertices after expanding the Lagrangian up to order $1/M_\Omega^2$.

(ii) Some effective operators give derivatives on the standard model fermion fields. These are not negligible, since they only vanish if the Dirac equation $i\not{\partial}\psi = m\psi$ can be used and the fermion mass m is small. This is not the case for e.g., heavy quark contributions in the annihilation sector and processes with off-shell fermions.

(iii) We use the same list of effective operators for the cases of real scalar ($\chi = \chi^\dagger$), real vector ($\chi_\mu = \chi_\mu^\dagger$) or Majorana fermion [41] dark matter fields. However, we would like to mention that for consistency we do not introduce additional factors of 1/2 in the couplings as is often done in the case of real fields.

C. Benchmark models

The effective operators described above have multiple independent parameters to describe the effective coupling, for example g_χ, g_l, g_r and M_Ω in the scalar dark matter, vector mediator (SV) case or g_s, g_p and M_Ω in the fermion dark matter, scalar mediator (FS) case in Table I.

Considering the full range of parameters would lead to a plethora of scenarios, well beyond the scope of this paper. Thus we restrict our analysis to specific benchmark models (see Table II) with constraints on the individual couplings such that only one overall multiplicative factor remains. The effective coupling constant G for each model is then defined as $G \equiv g_i g_j / M_\Omega^2$.

When comparing different experimental approaches to dark matter, a large dependence can be seen on the size of the interaction to different SM particles. We shall consider two cases for the set of SM particles that interact with dark matter: (i) all leptons (ii) all SM fermions. In addition, two variants of coupling strength are chosen. In one scenario all SM particles couple with the same strength; this is called *universal coupling*. In the second they have a coupling proportional to their mass, which we call *Yukawa coupling*. Since the latter strongly enhances dark matter couplings to the top quark, NLO contributions gain extra weight and might become dominant effects. This is particularly true for models that include fermion vector bilinears $\bar{\psi}\gamma^\mu\psi$, for which a virtual top quark pair can already be produced at 1-loop level through additional photon or gluon radiation. For those we expect significant deviations from the tree-level approximation and a full NLO description might be necessary to derive reasonable results here. We therefore omit the Yukawa-case for this class of models. However, models with only (pseudo)scalar or axialvector bilinears need at least 2 loops to get a nonvanishing matrix element. We expect these contributions to be suppressed strongly enough to keep the tree level approximation valid.

For models with fermionic mediators, the leading term has only a $1/M_\Omega$ dependence, which is why we define $G \equiv g_i g_j / M_\Omega$ for these. We also choose two possible values for M_Ω to represent different suppression scales of the respective second order terms. Models with real fields that are trivially connected to the corresponding complex cases by multiplicative prefactors are not taken into account separately. We also omit models with left-handed couplings that are related to the respective right–coupled cases. Information on these can easily be extracted from the related models by rescaling the corresponding result accordingly.

D. Consistency of models

We have chosen to include all possible combinations of spin (0, 1/2, 1) for the mediator and dark matter candidate so that our results can be compared with the full range of operators already consider in the literature e.g.,

TABLE I. List of interaction vertices for S(calar), F(ermion) and V(ector) dark matter, χ, before and after integrating out the heavy mediator scalar field ϕ, spinor field η or vector field Z^μ with mass M_Ω. ψ denotes the standard model fermion. $\partial X^{\mu\nu} \equiv \partial^\mu X^\nu - \partial^\nu X^\mu$. Fermionic tS and tV models denote cases where the mediator is exchanged in the t-channel. Note that all Lagrangians are hermitian by construction.

DM	Med.	Diagram	$-\mathcal{L}_{\rm UV}$ $-\mathcal{L}_{\rm eff}$
S	S	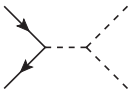	$g_\chi \chi^\dagger \chi \phi + \bar{\psi}(g_s + i g_p \gamma^5)\psi\phi$ $\frac{g_\chi}{M_\Omega^2}\chi^\dagger\chi\bar{\psi}(g_s + i g_p\gamma^5)\psi$
S	F	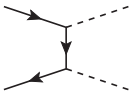	$\bar{\eta}(g_s + g_p\gamma^5)\psi\chi + \bar{\psi}(g_s - g_p\gamma^5)\eta\chi^\dagger$ $\frac{1}{M_\Omega}[(g_s^2 - g_p^2)\bar{\psi}\psi\chi^\dagger\chi + \frac{i}{M_\Omega}\chi^\dagger\bar{\psi}(g_s^2 + g_p^2 - 2g_s g_p\gamma^5)\gamma^\mu\partial_\mu(\psi\chi)]$
S	V	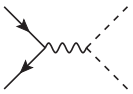	$g_\chi(\chi^\dagger\partial_\mu\chi - \chi\partial_\mu\chi^\dagger)Z^\mu + \bar{\psi}\gamma^\mu(g_l P_L + g_r P_R)\psi Z_\mu$ $\frac{g_\chi}{M_\Omega^2}\bar{\psi}\gamma^\mu(g_l P_L + g_r P_R)\psi(\phi^\dagger\partial_\mu\phi - \phi\partial_\mu\phi^\dagger)$
F	S	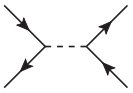	$\bar{\chi}(g_{s1} + g_{p1}\gamma^5)\chi\phi + \bar{\psi}(g_{s2} + g_{p2}\gamma^5)\psi\phi$ $\frac{1}{M_\Omega^2}\bar{\chi}(g_{s1} + i g_{p1}\gamma^5)\chi\bar{\psi}(g_{s2} + i g_{p2}\gamma^5)\psi$
F	V	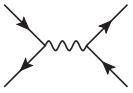	$\bar{\psi}\gamma^\mu(g_{l1}P_L + g_{r1}P_R)\psi Z_\mu + \bar{\chi}\gamma^\mu(g_{l2}P_L + g_{r2}P_R)\chi Z_\mu$ $\frac{1}{M_\Omega^2}\bar{\psi}\gamma^\mu(g_{l1}P_L + g_{r1}P_R)\psi\bar{\chi}\gamma_\mu(g_{l2}P_L + g_{r2}P_R)\chi$
F	tS	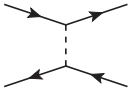	$\bar{\chi}(g_l P_L + g_r P_R)\psi\phi + \bar{\psi}(g_l P_R + g_r P_L)\chi\phi$ $\frac{1}{M_\Omega^2}\bar{\psi}(g_l P_R + g_r P_L)\chi\bar{\chi}(g_l P_L + g_r P_R)\psi$
F	tV	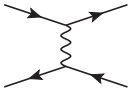	$\bar{\psi}\gamma^\mu(g_l P_L + g_r P_R)\chi Z_\mu + \bar{\chi}\gamma^\mu(g_l P_L + g_r P_R)\psi Z_\mu$ $\frac{1}{M_\Omega^2}\bar{\psi}\gamma^\mu(g_l P_L + g_r P_R)\chi\bar{\chi}\gamma_\mu(g_l P_L + g_r P_R)\psi$
V	S	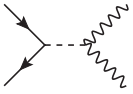	$-g_\chi\chi^\mu\chi_\mu\phi + \bar{\psi}(g_s + i g_p\gamma^5)\psi\phi$ $-\frac{g_\chi}{M_\Omega^2}\chi^\mu\chi_\mu\bar{\psi}(g_s + i g_p\gamma^5)\psi$
V	F	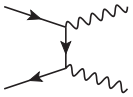	$-\bar{\eta}\gamma^\mu(g_l P_L + g_r P_R)\chi_\mu + \bar{\psi}\gamma^\mu(g_l P_L + g_r P_R)\eta\chi_\mu^\dagger$ $\frac{1}{M_\Omega}[g_l g_r\bar{\psi}\gamma^\nu\gamma^\rho\psi\chi_\nu^\dagger\chi_\rho + \frac{i}{M_\Omega}\chi_\nu^\dagger\bar{\psi}\gamma^\nu\gamma^\mu\gamma^\rho(g_l^2 P_L + g_r^2 P_R)\partial_\mu(\psi\chi_\rho)]$
V	V	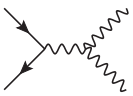	$i g_\chi[Z_\mu\chi_\nu^\dagger\partial\chi^{\mu\nu} + Z_\mu\chi_\nu\partial\chi^{\mu\nu} + \chi_\mu^\dagger\chi_\nu\partial Z^{\mu\nu}] + \bar{\psi}\gamma_\mu(g_l P_L + g_r P_R)\psi Z^\mu$ $\frac{i g_\chi}{M_\Omega^2}\bar{\psi}\gamma^\mu(g_l P_L + g_r P_R)\psi[\chi^\nu\partial\chi_{\mu\nu}^\dagger - \chi^{\dagger,\nu}\partial\chi_{\mu\nu} + \partial^\nu(\chi_\nu^\dagger\chi_\mu - \chi_\mu^\dagger\chi_\nu)]$

Refs. [18–23,26,36,38,39]. We would also like to make clear that our models should not be considered full ultraviolet completions to the standard model. Instead they are meant to illustrate the possible dominant interactions that dark matter may have with standard model fermions.

Nevertheless, some of the new interactions included may induce SU(2) violating couplings or additional forms of electroweak symmetry breaking. However we choose not to ignore these models since a full high energy theory may include cancellations that alleviate these issues. In

TABLE II. Benchmark models with specific values for the coupling constants shown in Table I. In the case of "FS" and "FV," the couplings "1" and "2" are always set equal.

Operators	Definition	Name
SS, VS, FS,	$g_p = 0$	scalar
	$g_s = 0$	pseudoscalar
SF, SFr:	$g_p = 0$, $M_\Omega = 1$ TeV	scalar_low
	$g_p = 0$, $M_\Omega = 10$ TeV	scalar_high
	$g_s = 0$, $M_\Omega = 1$ TeV	pseudoscalar_low
	$g_s = 0$, $M_\Omega = 10$ TeV	pseudoscalar_high
SV, FV, FtV,	$g_l = g_r$	vector
FtVr, VV:	$g_l = -g_r$	axialvector
	$g_l = 0$	right–handed
FtS, FtSr:	$g_l = g_r$	scalar
	$g_l = -g_r$	pseudoscalar
VF, VFr:	$g_l = g_r$, $M_\Omega = 1$ TeV	vector_low
	$g_l = -g_r$, $M_\Omega = 10$ TeV	vector_high
	$g_l = g_r$, $M_\Omega = 1$ TeV	axialvector_low
	$g_l = -g_r$, $M_\Omega = 10$ TeV	axialvector_high
FVr:	$g_l = 0$	right-handed

order to be more concrete, we now now list some of the problems that the full high energy may introduce:

(i) For any model with a single t-channel mediator that couples to more than one standard model particle, the interaction will violate some combination of lepton flavor, quark flavor and gauge charges. A solution to this problem is to relax the constraint that we have a single mediator and instead consider the possibility that there exists a degenerate set of intermediate particles in the model. A motivation for this kind of model comes from SUSY where a spectrum of degenerate squarks and sleptons would lead to this phenomenology.

(ii) Any model with an s-channel scalar mediator either violates isospin symmetry or the mediator has to carry SU(2) charge. In the second case dark matter also has to be charged under SU(2). Consequently it now has the possibility to interact with both the Z and the Higgs boson. A similar argument holds for hypercharge. Since those particles have a relatively low mass, the effective approach put forward in this paper is no longer strictly valid. For low momentum exchanges, these interactions can be expected to be dominant and thus our results are no longer reliable for direct detection, relic density or indirect detection. However, in case of the ILC a large coupling to the new mediator may still mean that this interaction is dominant and could give relevant bounds.

(iii) Similarly, for t-channel interactions the mediator has to carry appropriate quantum numbers to allow for a consistent coupling to standard model fermions. In case of a bosonic mediator, one mediator can only couple either to left or to right handed fermions because of their differing gauge charges. However, again a mass degenerate set of mediators with different quantum numbers could lead to mixed left-right-interacting scenarios. If the mediator itself is a fermion, its chiral components have to be put into different standard model gauge representations in order to give valid couplings. In all these cases, it can be made sure that dark matter keeps its singlet nature and does not interact with any additional standard model particles.

(iv) In the case of an SU(2) violating coupling, new forms of electroweak symmetry breaking and contributions to electroweak precision measurements can be expected. However, as stated above since we do not have the complete high energy theory it is impossible to know if these contributions can be cancelled by some additional states in the theory. Thus we include all possible models for completeness.

(v) When we introduce vector dark matter models we simply add the particle by hand with a set mass. Evaluating the high energy cross section at the ILC leads to terms with leading s/M_χ^4 dependence and for small dark matter masses these are divergent. Since only spontaneously broken gauge theories can lead to a consistent theory with massive vector particles [42] our phenomenological models cannot constitute a full theory. However, one can still find perturbatively valid results for mass ranges that do not violate unitarity and we study these bounds.

III. ASTROPHYSICAL CONSTRAINTS

Any model which aims to describe dark matter, for example through a WIMP, has to agree with present data. It has to give the correct relic abundance, and must be consistent with the bounds from direct and indirect detection searches [43–45].

A. The relic abundance

We first consider the best measurement of the relic abundance from WMAP-7 [43],

$$\Omega^{\mathrm{DM}} h^2 = 0.1099 \pm 0.0056. \tag{7}$$

We employ the solution of the model dependent Boltzmann equation obtained in Ref. [35],

$$\Omega_0^{\mathrm{DM}} h^2 \approx 1.04 \times 10^9 \ \mathrm{GeV}^{-1} \frac{x_f}{m_{\mathrm{Pl}} \sqrt{g_*(x_f)} (a + 3b/x_f)}. \tag{8a}$$

Here m_{Pl} is the Planck mass. $x_f = M_\chi / T_f$ is the inverse freeze-out temperature, T_f, rescaled by the WIMP mass, M_χ. It is implicitly given by the equation,

$$x_f = \ln\left[c(c+2)\sqrt{\frac{45}{8}}\frac{1}{2\pi^3}\frac{g m_{\rm pl} M_\chi (a+6b/x_f)}{\sqrt{x_f}\sqrt{g_*(x_f)}}\right]. \quad (8b)$$

$g_*(x_f)$ denotes the relativistic degrees of freedom in equilibrium at freeze-out and is given in Ref. [46]. a and b are the first two coefficients of the nonrelativistic expansion of the thermally averaged annihilation cross section,

$$\langle \sigma v \rangle \approx a + b v^2 + O(v^4), \quad (9)$$

where v is the relative velocity of the colliding particles. Here the center-of-mass energy squared is approximated by [38,39],

$$s \approx 4M_\chi^2 + M_\chi^2 v^2 + 3/4 M_\chi^2 v^4. \quad (10)$$

g are the internal degrees of freedom of the WIMP. c is an order unity parameter which is determined numerically in the solution of the Boltzmann equation and we set this parameter to 0.5. In the cases where we have the same effective operator our results agree with Refs. [38,39], up to the normalization (see Appendix A).

In order to set constraints, we must determine the total relic density, which is the sum of the relic density of the particle and the antiparticle (if the latter exists). This means the relic density for a complex particle-pair is two times the density of a real particle. If we consider the WMAP result as an upper bound on the relic density, i.e., allowing for other dark matter, then this corresponds to a lower bound on the effective coupling of the WIMP to the SM particles. If we require our WIMP to be the only dark matter, we shall also obtain an upper bound on the effective coupling.

The strict interpretation that our model only contains a heavy mediator and a single WIMP ensures that there are no resonances or coannihilations. However we also note that in many full theories that contain dark matter, a ''coannihilation'' regime can exist that can significantly alter the relic density in the universe. Whilst the coannihilation mechanism cannot be incorporated into the strict definition of our model, it may actually have no observable effect on the collider based phenomenology. An example of such a feature could be stau coannihilation in SUSY that would not change the ILC production process of the lightest supersymmetric particle. Another example is that a more complicated model may contain resonant annihilations. Both of these examples can significantly weaken the relic abundance bounds.

B. Direct detection

We shall also impose bounds on our operators from the direct detection searches for WIMP dark matter. The experiments are designed to measure the recoil energy from the scattering between a (dark matter halo) WIMP and the target nucleus. The interactions are difficult to detect since the energy deposited is quite small, 1 to 100 KeV, [1]. These experiments give an upper limit for the cross section between the dark matter and the nucleus of the target. One drawback is that in the cases where the WIMP does not couple to quarks, the coupling can only occur through loop diagrams.

The direct detection experiments give a much stronger bound on spin independent (SI) interactions than on spin dependent (SD). The reason is that in the SI case the interaction with all nucleons add coherently which enhances the corresponding cross section by the atomic number squared. However, the spins of the nucleons cancel if they are paired. Thus SD interactions are only enhanced for very special nuclei.

The SI interactions are scalar or vector interactions in the s-channel, the axialvector and tensor interactions in the s-channel give a SD interaction. Note that due to the low kinetic energy of the WIMPs the cross section should be computed in the nonrelativistic limit. In that case the pseudoscalar interaction, $\bar{\psi}\gamma^5\psi$, vanishes.

The t/u-channel diagrams are cast into a sum of s-channel diagrams via the Fierz identities. From this only the SI parts are employed, since any SD contribution is negligibly small. Tensor interactions occur only via the Fierz identities, since we do not consider fundamental tensor interactions. However, since Fierz identities will always give at least one SI contribution, tensor terms can be dropped.

For the SI interactions we shall consider the limits set by the XENON experiment [44]. These are the most recent and set the strictest limits over a broad parameter range. For the SD interactions we consider the XENON10 data [47] since XENON100 gives no statement on SD interactions. The smaller data set along with the physical reasons mentioned above lead to a bound that is $\sim 10^6$ times weaker than for the SI interactions. The calculations for the WIMP-nucleus cross sections follow Ref. [36] and for identical models we find the same results. See Appendix B for the complete list of cross sections.

C. Indirect detection

We also consider the indirect detection searches for dark matter. These are much more model dependent, as the dark matter is seen via an agent, for example neutrinos, which could also be produced via other means. Specifically we shall consider the PAMELA experiment [45] which measured an excess of positrons that could potentially originate from dark matter annihilation.

To implement this we need to compute the propagation of the produced positrons and electrons from the source to the earth. This is described by the diffusion-loss equation [48],

$$\frac{\partial \psi}{\partial t} - \nabla[K(\mathbf{x}, E)\nabla\psi] - \frac{\partial}{\partial E}[b(E)\psi] = q(\mathbf{x}, E). \quad (11)$$

Here $\psi(x, E) = {\rm d}n_{e^+}/{\rm d}E$ is the positron density per energy. $K(x, E)$ is the diffusion coefficient which describes

the interaction with the galactic magnetic field. $b(E)$ denotes the energy loss due to synchrotron emission and inverse Compton scattering. $q(x, E)$ is the source term due to dark matter annihilation. We note that convection and reacceleration terms are ignored as these do not apply to positrons [49].

We use the conventional formalism [50,51] to derive a solution of Eq. (11). It is also possible to use the so-called extended formalism that takes the corrections from sources in the free propagation zone into account as well as those from the diffusion zone. However, this increases the runtime of the calculation considerably while only giving a small correction that is less than the measurement error. To perform the numerical comparison we use the cored isothermal dark matter density profile [52] and the galactic propagation model M2 [50].

The above choices result in the following positron flux,

$$\Phi_{e^+}(E) = \frac{\beta_{e+}}{4\pi}\psi(r_\odot, z_\odot, E), \tag{12}$$

$$\psi(r, z, E) = \frac{\tau_E}{\epsilon^2}\int_\epsilon^{\epsilon_{\max}} d\epsilon_S f(\epsilon_S) I(r, z, \epsilon, \epsilon_S), \tag{13}$$

$$I(r, z, \epsilon, \epsilon_S) = \sum_i \sum_n J_0\left(\frac{\alpha_i r}{R}\right) \times \sin\frac{n\pi(z+L)}{2L}\exp\left(-\omega_{i,n}(t - t_S)\right)R_{i,n}, \tag{14}$$

$$\omega_{i,n} = K_0\left[\left(\frac{\alpha_i}{R}\right)^2 + \left(\frac{n\pi}{2L}\right)^2\right]. \tag{15}$$

Here τ_E, R, K_0, L are parameters which describe the M2 propagation model. They are set to the standard choices [50,51] $\tau_E = 10^{16}$ s, $R = 20$ kpc as well as to the M2 propagation model $L = 1$ kpc, $K_0 = 0.00595$ kpc^2/Myr, $\delta = 0.55$. $f(\epsilon)$ is the energy distribution of the positrons from the annihilation and is generated with PYTHIA8 [53]. $R_{i,n}$ are the coefficients of the Bessel-Fourier expansion of $R(r, z)$,

$$R(r, z) \equiv \eta\langle\sigma v\rangle\left[\frac{\rho(r, z)}{M_\chi}\right]^2, \tag{16}$$

$$\rho(r, z) = \rho_\odot\left(\frac{r_\odot}{r}\right)^\gamma\left[\frac{1 + (r_\odot/r_s)^\alpha}{1 + (r_\odot/r)^\alpha}\right]^{(\beta-\gamma)/\alpha}. \tag{17}$$

Here $\langle\sigma v\rangle$ is the thermally averaged annihilation cross section. We include all possible final states, not just those resulting in positrons. Furthermore $\eta = 1/2$ for real particles and $1/4$ for complex particles. $r_\odot = 8.5$ kpc is the distance of the solar system from the galactic center. $\rho_\odot = 0.3$ GeV\cm^3 is the local dark matter density and $\alpha = \beta = 2$, $\gamma = 0$, $r_S = 5$ kpc are chosen according to the cored isothermal dark matter density distribution [50,51].

PAMELA measures the ratio $\Phi_{e^+}/(\Phi_{e^-} + \Phi_{e^+})$, where the fluxes, $\Phi_{e^\pm}$, contain the flux from dark matter annihilation and from any astrophysical background. The background we take is [48]

$$\frac{d\Phi_{e^-bg}}{dE} = \left(\frac{0.16\epsilon^{-1.1}}{1 + 11\epsilon^{0.9} + 3.2\epsilon^{2.15}} + \frac{0.7\epsilon^{0.7}}{1 + 110\epsilon^{1.5} + 600\epsilon^{2.9} + 580\epsilon^{4.2}}\right)\text{GeV}^{-1}\,\text{cm}^{-2}\,\text{s}^{-1}\,\text{sr}^{-1}, \tag{18a}$$

$$\frac{d\Phi_{e^+bg}}{dE} = \frac{4.5\epsilon^{0.7}}{1 + 650\epsilon^{2.3} + 1500\epsilon^{4.2}}\,\text{GeV}^{-1}\,\text{cm}^{-2}\,\text{s}^{-1}\,\text{sr}^{-1}, \qquad \epsilon \equiv E/\text{GeV}. \tag{18b}$$

The quantity we compare to PAMELA is

$$\frac{\Phi_{e^+}}{\Phi_{e^+} + \Phi_{e^-}} = \frac{\Phi_{e^+\chi} + \Phi_{e^+bg}}{\Phi_{e^+bg} + \Phi_{e^+\chi} + \Phi_{e^-\chi} + \Phi_{e^-bg}}, \tag{19}$$

and we note that $\Phi_{e^+\chi} = \Phi_{e^-\chi}$.

We find an upper bound on the annihilation cross section by assuming that all of the excess comes from dark matter. However, it is possible that other background sources contribute and thus we also allow models that produce a flux smaller than the one seen.

In addition to constraining models of dark matter from the positron flux, PAMELA also measures the antiproton flux. For models that couple to quarks, these bounds can be very constraining [54] but since we are primarily interested in a direct correspondence with the ILC, we do not consider these.

We also note that for dark matter masses above ~1 TeV, the FERMI-LAT [55] experiment may provide competitive bounds from inverse Compton scattering [56,57]. However, since we are only interested in models that can be probed at the ILC we ignore them here. In the case of Majorana dark matter, hard photon emission from bremsstrahlung may also offer a possibility to probe these models but we do not consider this here [58].

The ICECUBE Collaboration also sets limits on heavier dark matter masses via annihilations into neutrino final states [59,60]. In addition these bounds may be competitive for spin dependent interactions but we do not consider the limits in this study.

IV. DARK MATTER SEARCH AT THE ILC

A. Radiative production of dark matter

For the ILC search, we look at the process $e^+e^- \to \chi\chi\gamma$ with a hard photon being the only detected particle in the final state, Fig. 1. We determine the polarized differential

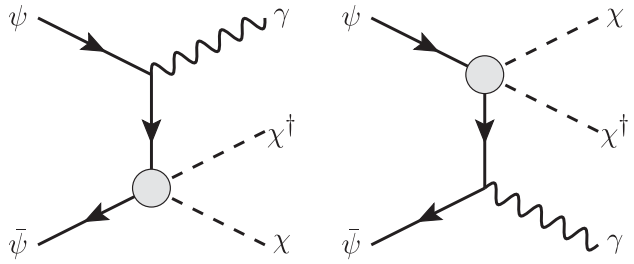

FIG. 1. Diagrams for radiative pair production of dark matter. Terms in which the heavy mediator can emit a photon are neglected.

cross section for this process with respect to the relative photon energy $x \equiv 2E_\gamma/\sqrt{s}$ and its polar angle θ by integrating over the full phase space of the final state dark matter particles. The results for this calculation are given in Table III, with further explanation of the abbreviations used given in Appendix C 1. Previous ILC studies, e.g., Refs. [9,14], have used the Weizsäcker-Williams approximation for soft photons. This formula relates the differential photon cross section to the total pair production cross section $e^+e^- \to \chi\chi$ with a reduced center of mass energy $s \to \hat{s} \equiv s(1-x)$ and multiplied by the kinematical function $F_{x\theta}$,

$$\frac{d\sigma[e^+e^- \to \bar{\chi}\chi\gamma]}{dx\,d\cos\theta_\gamma} \approx F_{x\theta}\hat{\sigma}[e^+e^- \to \bar{\chi}\chi]. \tag{20}$$

Due to the soft collinear approximation used, we expect that the above equation will perform poorly for large angle and high p_T photons. We compare the analytical result to this approximation to test the reliability. In Table III we put terms in bold, which are purely caused by our analytical treatment. The corrections are either of the form of an additional kinematical factor $V_{x\theta}$, mostly appearing in models with vector mediators, or completely new terms that typically appear in t-channel interactions. Since $\lim_{x\to 0} V_{x\theta} = 1$ and $\lim_{x\to 0}(A_i) = 0$, the WW-approximation is in agreement with our full result for small energies. In Fig. 2 we show the respective photon energy distributions for different models in both the WW-approximation and the full analytical treatment. The curves behave quite congruently with differences visible in the high energy sector. Since most of the signal events lie in the low energy part, the approximation gives accurate results for counting experiments. A shape dependent analysis would need to use the analytical result to estimate the correct threshold behavior for high energies. Our subsequent analysis is performed with the full analytical cross section.

TABLE III. Analytical differential cross sections for the process $e^+e^- \to \chi\chi\gamma$ in the various effective models. Terms in bold do not appear in the Weizsäcker-Williams approach and are given in Appendix C 1 where we also define all used abbreviations. Models with a suffix "r" correspond to the case of real particles. Cross sections for SSr, FSr and VSr are twice as large as in the complex case while SV and VV vanish completely for real particles.

Model	$\frac{d\sigma}{dx\,d\cos\theta}$
SS	$\frac{\hat{\beta}F_{x\theta}}{32\pi M_\Omega^4} G_{s+p} g_\chi^2 C_s$
SF	$\frac{\hat{\beta}F_{x\theta}}{32\pi M_\Omega^2}[G_{s-p}^2 C_s + \frac{\hat{\beta}^2\hat{s}}{12M_\Omega^2}\boldsymbol{V_{x\theta}}[(g_s+g_p)^4 C_R + (g_s-g_p)^4 C_L] + \boldsymbol{A}_{\mathrm{SF}}]$
SFr	$\frac{\hat{\beta}}{16\pi M_\Omega^2}[F_{x\theta} G_{s-p}^2 C_s + \boldsymbol{A}_{\mathrm{SFr}}]$
SV	$\frac{\hat{s}\hat{\beta}^3 F_{x\theta}}{96\pi M_\Omega^4}\boldsymbol{V_{x\theta}}[g_l^2 C_L + g_r^2 C_R] g_\chi^2$
FS	$\frac{\hat{s}\hat{\beta}F_{x\theta}}{16\pi M_\Omega^4} G_{s+p} C_s[g_s^2\hat{\beta}^2 + g_p^2]$
FV	$\frac{\hat{\beta}F_{x\theta}}{48\pi M_\Omega^4}\boldsymbol{V_{x\theta}}[G_{l+r}\hat{s}\hat{\beta}^2 + 3(g_l+g_r)^2 M_\chi^2][g_l^2 C_L + g_r^2 C_R]$
FVr	$\frac{\hat{s}\hat{\beta}^3 F_{x\theta}}{48\pi M_\Omega^4}\boldsymbol{V_{x\theta}}(g_l-g_r)^2[g_l^2 C_L + g_r^2 C_R]$
FtS	$\frac{F_{x\theta}\hat{\beta}}{48\pi M_\Omega^4} G_{l+r}^2[\boldsymbol{V_{x\theta}}(\hat{s}-M_\chi^2) + \boldsymbol{A}_{\mathrm{FtS}}]$
FtSr	$\frac{\hat{\beta}F_{x\theta}}{192\pi M_\Omega^4} G_{l+r}^2[3(\hat{s}-2M_\chi^2)C_P + \boldsymbol{V_{x\theta}} 2(\hat{s}-4M_\chi^2)C_V]$
FtV	$\frac{\hat{\beta}F_{x\theta}}{48\pi M_\Omega^4}[6G_{lr}^2 C_s(\hat{s}-2M_\chi^2) + (\hat{s}-M_\chi^2)\boldsymbol{V_{x\theta}}(g_l^4 C_L + g_r^4 C_R)]$
FtVr	$\frac{\hat{\beta}F_{x\theta}}{48\pi M_\Omega^4}[12G_{lr}^2 C_s(\hat{s}-2M_\chi^2) + (\hat{s}-4M_\chi^2)\boldsymbol{V_{x\theta}}(g_l^4 C_L + g_r^4 C_R)]$
VS	$\frac{\hat{\beta}F_{x\theta}}{128\pi M_\chi^4 M_\Omega^4} G_{s+p} g_\chi^2 C_s(12M_\chi^4 - 4M_\chi^2\hat{s} + \hat{s}^2)$
VF	$\frac{\hat{\beta}F_{x\theta}}{3840\pi M_\chi^4 M_\Omega^2}[40G_{lr}^2 C_s(7M_\chi^4 - 2M_\chi^2\hat{s} + \hat{s}^2) + \frac{1}{M_\Omega^2}(g_l^4 C_L + g_r^4 C_R)(40M_\chi^6 - 22M_\chi^4\hat{s} + 56M_\chi^2\hat{s}^2 + 3\hat{s}^3) + \boldsymbol{A}_{\mathrm{VF}}]$
VFr	$\frac{\hat{\beta}F_{x\theta}}{3840\pi M_\chi^4 M_\Omega^2}[60G_{lr}^2 C_s(12M_\chi^4 - 4M_\chi^2\hat{s} + \hat{s}^2) + \frac{1}{M_\Omega^2}(g_l^4 C_L + g_r^4 C_R)(320M_\chi^6 - 104^4\hat{s} + 32M_\chi^2\hat{s}^2 + \hat{s}^3) + \boldsymbol{A}_{\mathrm{VFr}}]$
VV	$\frac{\hat{s}\hat{\beta}^3 F_{x\theta}\boldsymbol{V_{x\theta}}}{3840\pi M_\chi^4 M_\Omega^4}[g_l^2 C_L + g_r^2 C_R] g_\chi^2(M_\chi^4 + 20M_\chi^2\hat{s} + \hat{s}^2)$

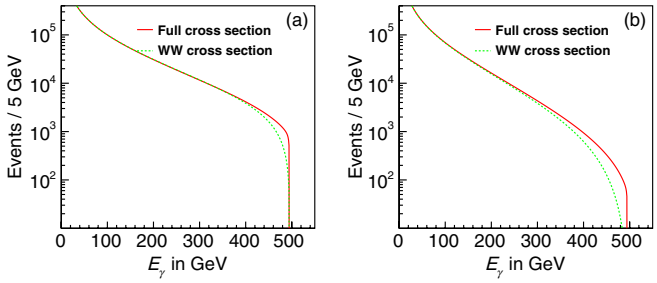

FIG. 2 (color online). Comparison of tree level photon energy distributions in the WW-approximation and the analytical solution for $M_\chi = 50$ GeV, $|\cos\theta_\gamma|_{\max} = 0.98$ and $\sqrt{s} = 1$ TeV. (a) SV, (b) FtS.

When we restrict the various couplings in our model according to the benchmark scenarios, Table II, most of the cross sections simplify and have only one polarization dependent term C_i. To determine the polarization leading to the best signal to background ratio, we only need to consider cases with different C_i. We therefore classify our models as follows:

$$\begin{aligned} \text{Scalar-like:}\sigma_{\text{pol}} &= C_S\sigma_{\text{unpol}}, \\ \text{Vector-like:}\sigma_{\text{pol}} &= C_V\sigma_{\text{unpol}}, \\ \text{Right-like:}\sigma_{\text{pol}} &= C_R\sigma_{\text{unpol}}, \\ \text{Left-like:}\sigma_{\text{pol}} &= C_L\sigma_{\text{unpol}}. \end{aligned} \tag{21}$$

Models with t-channel mediators usually have multiple terms with different polarization behavior and do not fall into one of the basic polarization classes given in Eq. (21). We choose the following polarization settings for those:

(i) Models with fermionic mediators are classified according to their leading term, which is always scalar-like.

(ii) All other models have both scalar-like and vector-like parts of about the same size. We analyze them in a vector-like scenario that naturally leads to a better background suppression.

B. Standard model background for monophotons

We consider the two leading dominant standard model background contributions after selection, determined with a full ILD (International Linear Detector concept) detector simulation [14,61]. All numbers here and in the following paragraphs refer to the nominal ILC center of mass energy of 500 GeV [62]. We also consider the case of an increased energy of 1 TeV and mention the differences later.

(i) Neutrinos from $e^+e^- \to \nu\bar{\nu}\gamma(\gamma)$ form a polarization dependent background. The leading contribution comes from t-channel W-exchange, which only couples to left-chiral leptons. Additional smaller contributions come from s-channel Z-diagrams with both left- and right-chiral couplings. We also consider the case of one additional undetected photon, which contributes with a size of roughly 10%.

(ii) Bhabha scattering of leptons with an additional hard photon, $e^+e^- \to e^+e^-\gamma$ has a large cross section but a very small selection efficiency, since both final state leptons must be undetected. It has been determined to give a contribution of the same order of magnitude as the neutrino background, after application of all selection criteria. It is mostly polarization independent [14,61].

Other background sources (like additional soft photons or photons faking electrons) contribute with less than 1% compared to the neutrino background and are therefore omitted [61].

C. Data modeling

To evade the use of a full detector simulation, we build on the results of Refs. [14,61]. For the signal and monophoton neutrino background, we generate the events by ourselves with the given phase space criteria. We then apply the ILD estimates for the energy resolution as well as the reconstruction and selection efficiencies[2] and compare the final energy distributions. For the diphoton neutrino and Bhabha background, we model the final distributions directly from the given results performed with a full detector simulation [14,61].

For the generation of signal and monophoton neutrino events we use CALCHEP [63]. We produce signal events for all benchmark scenarios with dark matter masses ranging from 1 to 240 GeV. To avoid collinear and infrared divergences, we limit phase space in the event generation to $E_\gamma \in [8\text{ GeV}, 250\text{ GeV}]$ and $\cos\theta_\gamma \in [-0.995, 0.995]$. Initial state radiation (ISR) and beamstrahlung significantly change the width and position of the neutrino Z^0-resonance, Fig. 3(a), and are taken into account. We set the accessible parameters in CALCHEP according to the ILD letter of intent [64] to 645.7 nm for the bunch size, 0.3 mm for the bunch length and a total number of particles per bunch of 2×10^{10}.

The finite resolution of the detector components and the use of selection criteria to reduce beam-induced background are taken into account by applying the following steps to both signal and background data. First, we shift the photon energy, given in GeV, according to a Gaussian distribution by taking into account the estimated resolution of the ILD detector components [64],

$$\frac{\Delta E_\gamma}{E_\gamma} = \frac{16.6\%}{\sqrt{E_\gamma \text{ in GeV}}} \oplus 1.1\%. \tag{22}$$

Afterwards we further limit the phase space to reduce background processes in the Z^0-resonance peak at 242 GeV and additional collinear photons from ISR,

[2]From here on, the expression "efficiency" abbreviates "reconstruction and selection efficiencies."

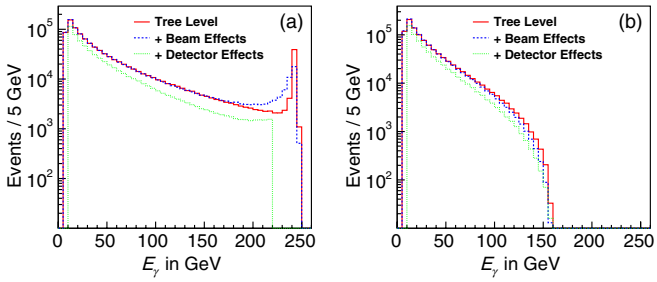

FIG. 3 (color online). Photon energy distribution before and after application of beam effects (ISR + beamstrahlung) and detector effects (resolution + efficiency) for (a) unpolarized neutrino background and (b) unpolarized FS scalar signal with $M_\chi = 150$ GeV. Distributions are normalised to 10^6 tree level events.

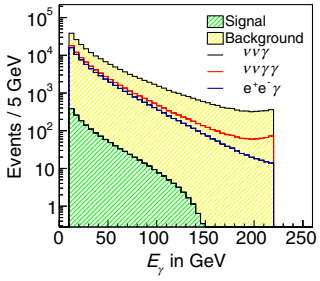

FIG. 4 (color online). Photon energy distributions of the most dominant background contributions (stacked) compared to an example signal (FS Scalar, $M_\chi = 150$ GeV) with a total cross section of 100 fb. All spectra are taken after selection for an unpolarized initial state.

$$E_\gamma \in [10\ \text{GeV}, 220\ \text{GeV}], \qquad \cos\theta_\gamma \in [-0.98, 0.98]. \tag{23}$$

The additional angular cut ensures a good photon reconstruction within the detector. Finally a random elimination of events is used to simulate the efficiency factor for reconstruction and selection determined in Ref. [61]. The efficiency consists of an energy dependent part ϵ_1 and a constant part ϵ_2 that are applied successively,

$$\begin{aligned} \epsilon_1 &= 97.22\% - (E_\gamma\ \text{in GeV}) \cdot 0.1336\%, \\ \epsilon_2 &= 96.8\%. \end{aligned} \tag{24}$$

Figure 3 shows how these settings affect the signal and background spectrum and Fig. 4 shows a stacked histogram of the dominant background processes along with a example dark matter signal. In Table IV we show how the total number of events in each of the background processes is affected by the incoming lepton polarization.

D. Analysis

We are interested in determining the upper bound on the effective coupling constants that the ILC can find for each individual model under the assumption that no signal events are measured. We perform a counting experiment by using the TROLKE [65] statistical test. We determine the total number of background events along with its statistical and systematic fluctuation ΔN_B and exclude coupling constants which would lead to a larger number of signal events than the 90% confidence interval of the background-only assumption.

TABLE IV. Total number of events in the different background sources after application of all selection criteria. The numbers are given for an integrated luminosity of 1 fb^{-1} in different polarization settings. Numbers in brackets are taken from Ref. [61] which employed a proper detector simulation.

P^-/P^+	$\nu\nu\gamma$	$\nu\nu\gamma\gamma$	$e^+e^-\gamma$
0/0	2257 (2240)	226 (228)	1218 (1229)
+0.8/ − 0.3	493 (438)	49 (43)	1218 (1204)
−0.8/ + 0.3	5104 (5116)	510 (523)	1218 (1227)

E. Systematic uncertainties

Systematic uncertainties play an important role in determining the total error on the background, ΔN_B, and for estimating the bounds on the effective couplings. There are two dominant contributions, motivated in Ref. [61] which we now discuss.

The experimental efficiency given in Eq. (24) will be determined at the real experiment by measuring the Z^0-resonance peak, which is theoretically known to a very good accuracy. Systematic uncertainties on that value are given by the finite statistics of this measurement and further broadening of the peak by unknown beam effects. These errors can be extrapolated down to the dark matter signal region at small photon energies and, since the same efficiency factor is used for signal and background, is highly correlated between those two. This global uncertainty will therefore approximately cancel in the determination of the maximum coupling G_{eff}.

Cancellation will not take place for model dependent effects however. This is due to the fact that the signal energy distribution depends on the unknown mass of the dark matter particle and the underlying interaction model. Therefore, the correct function $\epsilon(E_\gamma)$ for the signal will be different from the used neutrino background efficiency given in Eq. (24). Since we do not know the model a priori, we use the same value for both and introduce an error on the determination of the signal events, N_S. Compared to Ref. [61], we use a conservative value of $\Delta\epsilon = 2\%$.

Since the neutrino spectrum depends on the incoming lepton's polarization $P^\pm$, any fluctuation within those parameters will give additional systematic uncertainties on the number of expected background events. One cannot use the information from measuring the Z^0-resonance in this case to infer information in the low energy signal range because of the polarization dependence of the shape itself. Given the assumed accuracy of at least $\Delta P/P = 0.25\%$

TABLE V. Total amount of background events, N_B, with statistical error, Δ^{stat}, systematic error, Δ^{sys}, and the total error, Δ^{tot}. The subscripts 50 and 500 denote the integrated luminosity in inverse femtobarn. In case of a ten times larger luminosity, one will get ten times as many events in all channels; to better compare to the error of the low luminosity case, we give $\tilde{\Delta}^{stat}_{500} \equiv \Delta^{stat}_{50}/\sqrt{10}$. The polarization uncertainties are set to 0.25% (P) and 0.1% ($\tilde{P}$).

P^-/P^+	N_B	Δ^{stat}_{50}	$\tilde{\Delta}^{stat}_{500}$	Δ^{sys}_{P}	$\Delta^{sys}_{\tilde{P}}$	Δ^{tot}_{50P}	$\Delta^{tot}_{50\tilde{P}}$	$\tilde{\Delta}^{tot}_{500P}$	$\tilde{\Delta}^{tot}_{500\tilde{P}}$
0/0	184998								
+0.8/ + 0.3	97568	312	99	312	125	441	336	327	159
+0.8/ + 0.6	102365	320	101	385	154	500	355	398	184
+0.8/ − 0.3	87974	297	94	169	68	341	304	193	116
+0.8/ − 0.6	83177	288	91	104	42	307	291	138	100
−0.8/ + 0.3	341597	584	185	351	140	682	601	396	232
−0.8/ + 0.6	404970	637	201	501	200	811	668	546	284
−0.8/ − 0.3	212851	461	156	233	93	517	471	275	173
−0.8/ − 0.6	148478	385	122	337	135	512	408	359	182

[64] with a possible improvement to 0.1% at the ILC, we can derive the corresponding error on the polarized number of background events. As an example we show the left-handed background,

$$\frac{N_{pol}}{N_{unpol}} = (1 + P^+)(1 - P^-),$$
$$\frac{\Delta N_{pol}}{N_{unpol}} = \sqrt{[P^-(1 + P^+)]^2 + [P^+(1 - P^-)]^2}\,\frac{\Delta P}{P}. \quad (25)$$

From the numbers in Table IV, we assume an identical polarization dependence for $\nu\nu\gamma$ and $\nu\nu\gamma\gamma$ events and no dependence for the Bhabha background.

F. Polarization settings

Polarization can be used to significantly increase the number of signal events according to Eq. (21) but also increases the systematical contribution to the total background error, ΔN_B via Eq. (25). We are interested in the settings for each individual model that leads to the largest $N_S/\Delta N_B$ ratio allowing for the strictest bounds on G_{eff}. In Table V we give the total number of background events in different polarization settings $P^- = \pm 0.8$ and $P^+ = \pm 0.3/\pm 0.6$ that are feasible at the ILC [62]. We give the statistical fluctuation for integrated luminosities of 50 fb^{-1} as well as for 500 fb^{-1}. Since the latter will give ten times as much events in all channels, we reduce the statistical error accordingly to give a value comparable to the small luminosity case. We also give the systematic error that is dominated by the polarization uncertainty for two estimates of the polarization error $\delta P/P = 0.25\%$ and 0.1% [66]. Finally we give the total errors adding all combinations of individual errors in quadrature.

On the signal side, we look at the different classes derived in Sec. II with respect to their polarization dependence. For comparison, we use a common reference value of 500 unpolarized events for an integrated luminosity of 50 fb^{-1} and derive the corresponding number of events for polarized input.

We look for the maximum ratio $r \equiv N_S/\Delta N_B$ and the results for the best settings are displayed in Table VI. In most cases the largest possible polarization for the incoming leptons enhances the result. For high statistics and a nonreduced polarization error, the systematic uncertainty from increased polarization may outweigh the gain in the number of signal events though. In those cases, which appear only in scalar- and left-coupling models, less polarized beams lead to better results.

TABLE VI. Determination of the best ratio $r \equiv N_S/\Delta N_B$ with ΔN_B given by the different total errors determined in Table V. N_S describes the number of polarized signal events for the different classes described in Sec. II with a common reference value of 500 unpolarized events for an integrated luminosity of 50 fb^{-1}. We only show the polarization signs with the largest ratios. We mark the numbers which lead to the best signal to background ratio in bold.

IA type	P^-/P^+	N_S	r_{50P}	$r_{50\tilde{P}}$	r_{500P}	$r_{500\tilde{P}}$
Scalar	+0.8/+0.3	620	1.41	1.85	**1.90**	3.90
	+0.8/+0.6	740	**1.48**	**2.08**	1.86	**4.02**
Vector	+0.8/−0.3	620	1.82	2.04	3.21	5.34
	+0.8/−0.6	740	**2.41**	**2.54**	**5.36**	**7.40**
Left	−0.8/+0.3	1170	1.72	1.95	**2.95**	5.04
	−0.8/+0.6	1440	**1.78**	**2.16**	2.64	**5.07**
Right	+0.8/−0.3	1170	3.43	3.85	6.06	10.09
	+0.8/−0.6	1440	**4.69**	**4.95**	**10.43**	**14.4**

TABLE VII. Total amount of background events (N_B) and different error sources (see Table V) for $\sqrt{s} = 1$ TeV.

P^-/P^+	N_B	Δ^S_{50}	$\tilde{\Delta}^S_{500}$	δ^P_P	$\delta^P_{\tilde{P}}$	Δ^{tot}_{50P}	$\Delta^{tot}_{50\tilde{P}}$	$\tilde{\Delta}^{tot}_{500P}$	$\tilde{\Delta}^{tot}_{500\tilde{P}}$
0/0	162437								
+0.8/ + 0.3	54649	234	74	380	152	446	279	387	169
+0.8/ + 0.6	62791	251	79	469	188	531	314	476	203
+0.8/ − 0.3	38365	196	62	201	82	281	212	210	102
+0.8/ − 0.6	30223	174	55	125	50	214	181	137	74
−0.8/ + 0.3	357173	598	189	428	171	735	622	468	255
−0.8/ + 0.6	435979	660	209	612	245	900	704	647	322
−0.8/ − 0.3	199561	447	141	284	114	530	461	317	181
−0.8/ − 0.6	120755	348	110	411	165	538	385	425	198

TABLE VIII. Simulated and modeled number of events in the different background sources after application of all selection criteria for $\sqrt{s} = 1$ TeV. The numbers are calculated for an integrated luminosity of 1 fb^{-1} in different polarization settings.

P^-/P^+	$\nu\nu\gamma$	$\nu\nu\gamma\gamma$	e^+e^-
0/0	2677	268	304
+0.8/ − 0.3	421	42	304
−0.8/ + 0.3	6217	622	304

G. Increasing $\sqrt{s}$ to 1 TeV

We also consider the possibility of a doubled center of mass energy. This changes the previous analysis as follows:

(i) We generate events in a larger photon energy range $E_\gamma \in [8\ \text{GeV}, 500\ \text{GeV}]$ and reduce it to the interval $[10\ \text{GeV}, 450\ \text{GeV}]$ after performing the energy resolution shift $\Delta E/E$. This again reduces background events from the Z^0-resonance, which now is positioned at 496 GeV.

(ii) Dark matter signal processes can now be produced with masses up to 490 GeV.

(iii) We use our previously modeled distribution for the Bhabha background and rescale it by a factor of $1/4$, taking into account that the full cross section for that process is approximately proportional to $1/s$.

(iv) We use, as a rough approximation, the same ISR and beamstrahlung parameters in CALCHEP, efficiency factors and systematic error estimates.

Tables VII, VIII, and IX summarize again the number of background events per background scenario, the individual error sources and the determination of the best polarization setting for the increased center of mass energy. In contrast to the Bhabha cross section that falls mainly according to $\sigma \propto 1/s$, the neutrino background gets significant contributions from t-channel $W^\pm$s, which give s/m_W^4 -terms in the evaluation of the total cross section. The left-handed neutrino contribution therefore gets enhanced whereas the Bhabha background becomes less dominant in some polarization channels. This leads to a larger relative polarization error and therefore a larger impact on the size of the background fluctuation. In the end, vector- and right-coupling models receive stronger enhancement for polarized input than in the $\sqrt{s} = 500$ GeV case, whereas the other models suffer from the larger impact of polarization on the total error and prefer smaller polarization.

V. RESULTS

We begin by presenting the reach at the ILC in terms of the effective coupling constant in Sec. VA. We then compare these potential bounds with the couplings predicted by the cosmological relic density and the bounds coming from direct and indirect detection experiments. Of course we would also like to discover a dark matter at the ILC and the bounds provide an estimate of the potential sensitivity of the collider.

TABLE IX. Determination of the best ratio $r \equiv N_S/\Delta N_B$ (see Table VI) for $\sqrt{s} = 1$ TeV.

Model	P^-/P^+	N_S	r_{50P}	$r_{50\tilde{P}}$	r_{500P}	$r_{500\tilde{P}}$
Scalar	+0.8/+0.3	620	1.39	2.22	**1.60**	**3.7**
	+0.8/+0.6	740	**1.39**	**2.36**	1.55	3.65
Vector	+0.8/−0.3	620	2.21	2.92	2.95	6.08
	+0.8/−0.6	740	**3.46**	**4.09**	**5.40**	**10.00**
Left	−0.8/+0.3	1170	1.59	1.88	2.50	**4.59**
	−0.8/+0.6	1440	**1.60**	**2.05**	2.23	4.47
Right	+0.8/−0.3	1170	4.16	5.52	5.57	11.47
	+0.8/−0.6	1440	**6.73**	**7.96**	**10.51**	**19.46**

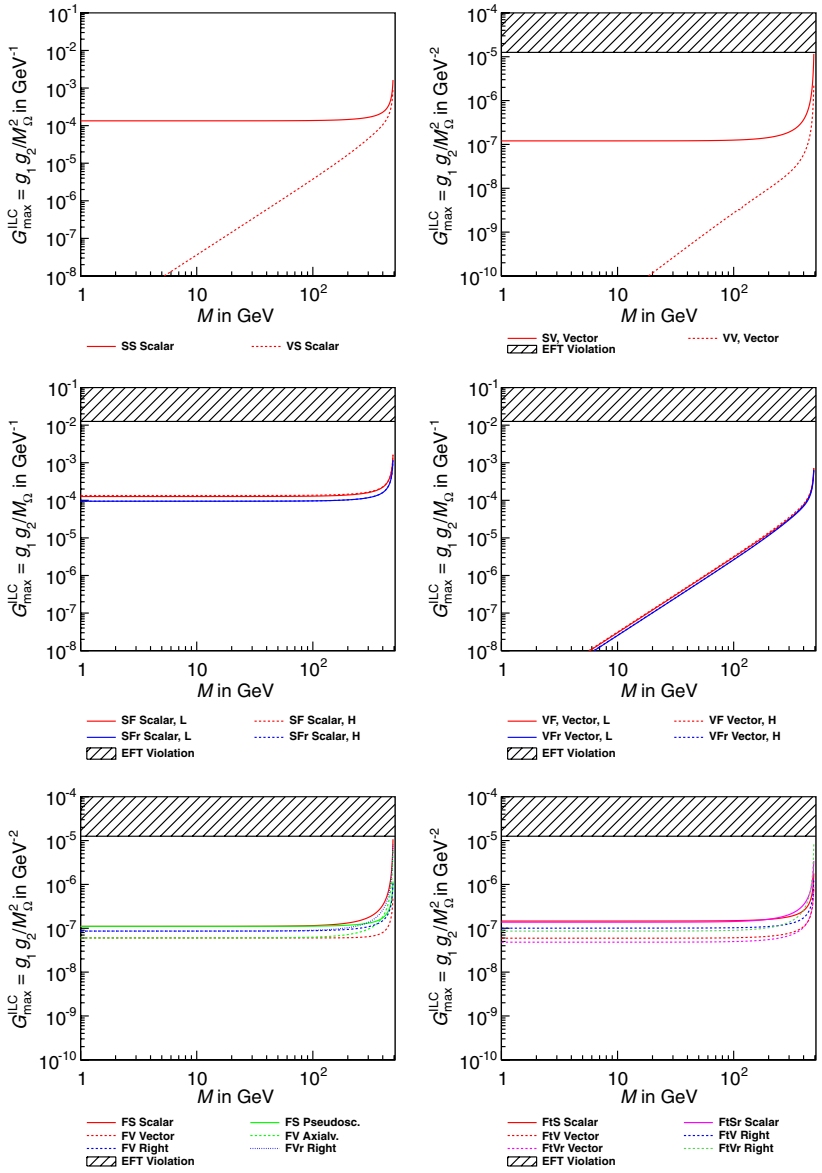

FIG. 5 (color online). 90% exclusion limits on the effective couplings accessible at the ILC with $\sqrt{s} = 1$ TeV. We only give effectively allowed regions for models with dimensionless fundamental couplings g.

A. ILC Bounds

We determine the 90% exclusion bound for the effective coupling constant in each benchmark model for the best case scenario. The integrated luminosity is set to 500 fb^{-1} and the systematic polarization error to $\Delta P/P = 0.1\%$. For each benchmark model we choose the polarization setting that leads to the best signal to background ratio for the corresponding polarization behavior according to Tables VI and IX. Results for different polarization settings can be found by rescaling the bound on the coupling according to $G' = G\sqrt{r'/r}$ with r denoting the ratio $N_S/\Delta N_B$ given in Table IX. We choose to present all of the results for an ILC with a center of mass energy of 1 TeV due to the increased range of dark matter masses that this option can probe. In addition, smaller effective couplings can be probed, mainly due to the falling Bhabha background.

In Fig. 5 we show the derived bounds on the coupling constants for an ILC center of mass energy of 1 TeV. The hashed area denotes the region that either violates the tree level approach with a too large dimensionless coupling constant $g^2 > 4\pi$, or by having a too small mediator mass $M_\Omega < 1$ TeV, for the effective approach to be valid. Note that the leading order in models with fermionic mediators has a different mass dimension and therefore gives a different definition for the effective coupling constant G_{eff}. If a model has no separate "pseudoscalar" or "axialvector" results, it is identical to the corresponding

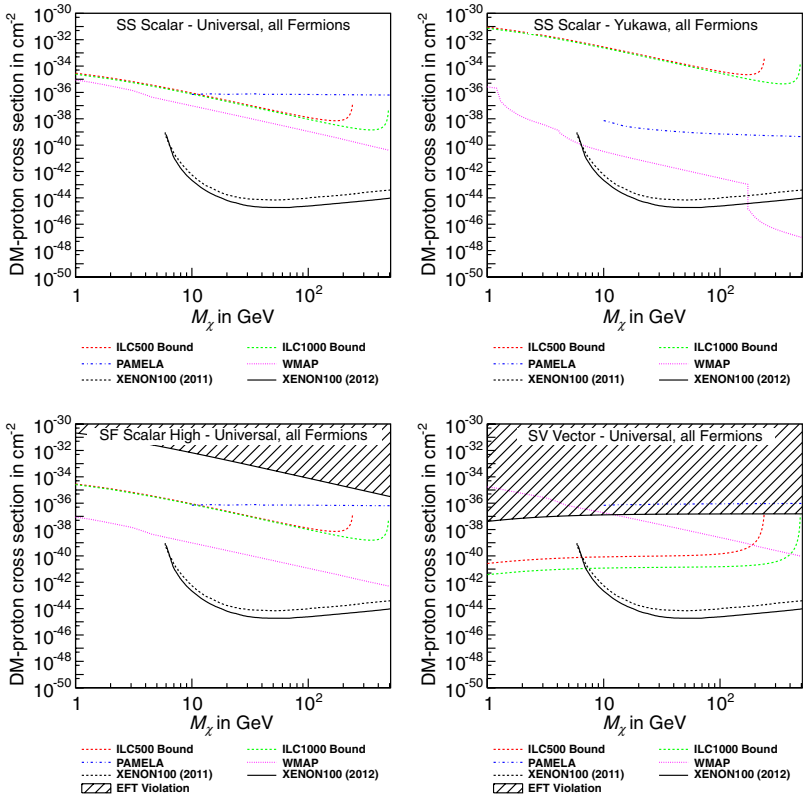

FIG. 6 (color online). Combined 90% exclusion limits on the spin independent dark matter proton cross section from ILC, PAMELA and WMAP for a selection of scalar dark matter models.

"scalar"/"vector" line due to identical cross section formulas. For masses away from the threshold, the ILC is able to exclude coupling constants down to the order of 10^{-7} GeV^{-2} or 10^{-4} GeV^{-1}, depending on the mass dimension. This corresponds to a total cross section (for the given phase space criteria) of about 0.3 fb. Exceptions however arise for models with vector dark matter that tend to have very strong exclusion limits for small masses. This is caused by the $1/M_\chi^4$ dependence in the photon cross section, which leads to divergences for very small vector boson masses. It has been shown [42] that only spontaneously broken gauge theories can lead to models with massive vector particles that are not divergent. Therefore, our initial fundamental model cannot be the full theory for all energies. In our effective approach, we restrict the energy to a maximum and in that case one can still receive perturbative valid results for mass ranges that do not violate unitary bounds. However, the perturbatively allowed mass range cannot be given in this model independent approach, since such an analysis needs more information about the size of the individual couplings and the relation between the mass of the mediator and the dark matter mass itself. In summary, a more detailed fundamental theory is needed to evaluate the breakdown of perturbation theory in this scenario.

We note that in models with fermionic operators, the subleading order has a negligible effect, as can be seen from the nearly identical lines for fermionic mediators with different masses.

B. Combined results

The combined maximum exclusion limits for spin independent DM-proton interaction at PAMELA, WMAP and the ILC are shown in Figs. 6–8. We choose a subset of models that couple to all standard model fermions and give an overview of the bounds that we can expect. Other models behave similarly and are therefore not shown again separately. We can give the following statements about the comparison of the ILC exclusion bound with the current XENON limits:

(i) We have sensitivity to spin independent proton cross sections for, as an example, the FV Vector model down to 10^{-42} cm^{-2} or equivalently 10^{-3} fb, which is an improvement of about four orders of magnitude compared to current LEP [33] and two orders of magnitude compared to current Tevatron [19] and CMS [31] results.

(ii) An increased center of mass energy can lead to stronger bounds by up to one order of magnitude. It also allows a larger dark matter mass range to be probed.

(iii) ILC bounds get significantly weakened if the interaction is Yukawa-like. At the ILC the mediator must couple to electrons, which have a suppressed

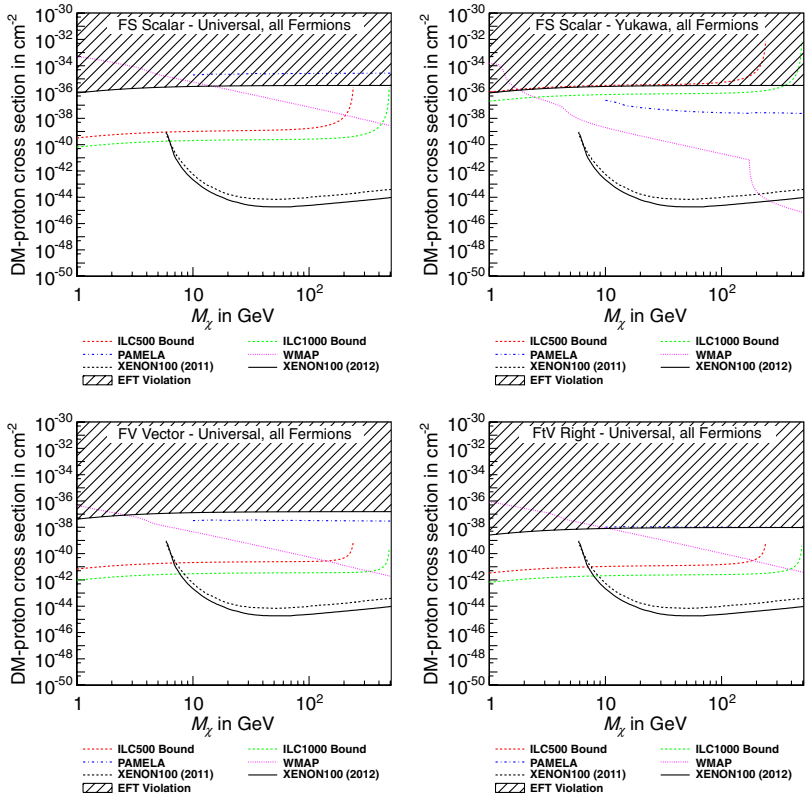

FIG. 7 (color online). Combined 90% exclusion limits on the spin independent dark matter proton cross section from ILC, PAMELA and WMAP for a selection of fermionic dark matter models.

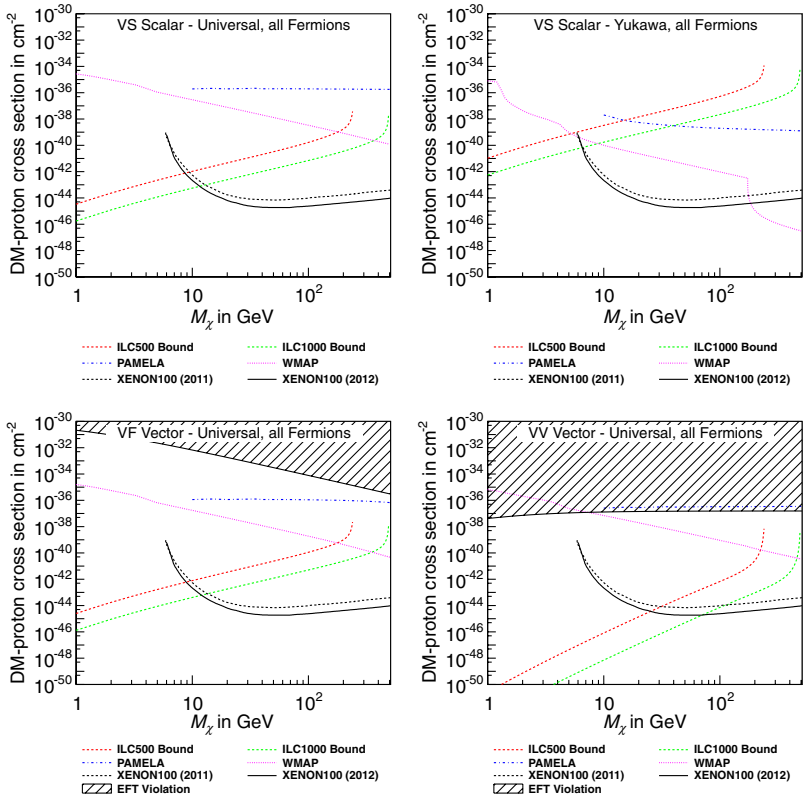

FIG. 8 (color online). Combined limits on the spin independent dark matter proton cross section from ILC, PAMELA and WMAP for a selection of vector dark matter models.

Yukawa coupling. The production cross section is thus small, leading to weaker bounds.

(iv) Models with scalar mediators give weaker bounds than models with vector interactions. For fermionic dark matter we observe a difference of about two orders of magnitude, which is in agreement with previously mentioned results from e.g., LEP. For scalar and vector dark matter the difference is mass-dependent and can increase to up to six orders of magnitude, which is due to the different mass dimension of the couplings.

(v) The WMAP bounds are for many effective models very constraining, Figs. 6–9. However, we would like to point out that these can be highly dependent on the full theory whilst not affecting the ILC or direct detection phenomenology. For example, annihilation can occur via some resonance or as in some SUSY models, coannihilation with staus or stops.

In Fig. 9 we show some models which allow for lepton couplings only. In that case, dark matter can only interact with protons via photons through a fermion loop, cf. Appendix. B 4. The loop factor significantly lowers the cross section and therefore increases the bound in the case of vector coupled models. Other models allow quark couplings only at the 2-loop level or theoretically completely forbid them [33]. In all cases, the ILC would give the strongest exclusion bounds for dark matter lepton couplings. For models with fermionic mediators there is an extra subtlety when comparing the bounds. In particular the exclusion limit at the ILC is mainly given by the leading term in the operator expansion, which is scalar like. Loop couplings can only happen for vector currents, which in the case of a fermionic mediator is only given by the subleading order and has an additional factor of $1/M_\Omega^2$. In that case, when translating any exclusion limits into bounds on the WIMP-proton cross section, we need to know the exact mass of the mediator. We show this in Fig. 9 for the two different chosen suppression scales "Low" ($M_\Omega = 1$ TeV) and "High" ($M_\Omega = 10$ TeV), Table II. In Fig. 10 we show the exclusion limits for the spin-dependent interaction. In our case, only the model with fermionic dark matter, a vector mediator and an axial-vector coupling leads to such an interaction. In that case, we compare with data from the previous XENON experiment (XENON10), since no results for the XENON100 phase were available when this study was completed. Since in this scenario dark matter only couples to a single nucleon on average because of the natural spin antialignment in nuclei, the XENON bounds are not coherently enhanced by the atomic number and therefore strongly lose sensitivity. The ILC would also give strongest

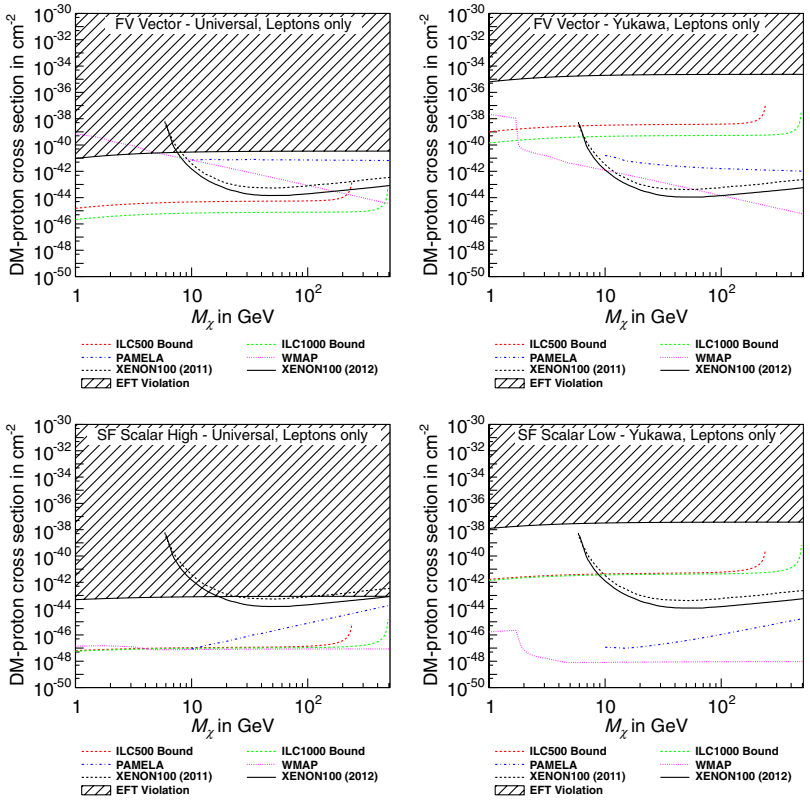

FIG. 9 (color online). Combined limits for a selection of models with loop-coupling to leptons only. "Low" corresponds to $M_\Omega = 1$ TeV and "High" to $M_\Omega = 10$ TeV, Table II.

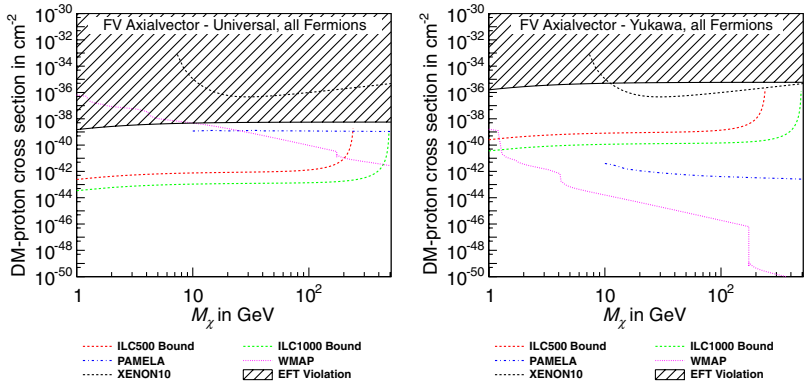

FIG. 10 (color online). Combined limits on the spin dependent dark matter proton cross section.

exclusion bounds over the whole accessible mass range here.

VI. CONCLUSIONS

In this paper we considered a broad range of effective models for dark matter and investigated the possibility that these models could be explored at the ILC. The models considered the possibility that dark matter was a new scalar, fermion or vector particle and would be produced at the ILC via a new, heavy intermediate state, the mediator particle. For the mediator we also considered spins 0, $1/2$ and 1. We obtained the corresponding effective theories by integrating out the mediator field.

To be able to compare the reach of the ILC with the other experimental searches, certain assumptions have to be made on how the mediator and dark matter couples to the standard model particles. We assume in all models that interactions only occur with the standard model fermions but the relative strength to different particles is varied. In the simplest variant we choose that the coupling is equal between all the standard model states. Another choice is that the interaction scales with the mass of the interacting standard model fermion, a ''Yukawa-like'' interaction. The last choice we make is the most optimistic for ILC phenomenology with only the standard model leptons interacting with the heavy mediator. Since the produced dark matter particles will be invisible to the ILC detectors, we require a radiated photon to be emitted from the initial state that will recoil against missing momentum. This topology provides a distinctive signal with which to discover dark matter. For the ILC study, we included the dominant backgrounds and most important detector effects. In addition we considered the possibility of using polarized initial states to reduce backgrounds and improve the signal strength.

The effective theories that we consider provide an efficient way to compare the reach of the ILC with other methods to discover dark matter. First, we consider the dark matter annihilation cross section required for the relic density observed by WMAP. We also look at the direct detection bounds at XENON by calculating the dark matter-nucleon scattering cross section. In addition, we include bounds from dark matter annihilation to positrons from the PAMELA experiment.

In terms of the effective dark matter model, we found that the ILC should be able to probe couplings 10^{-7} GeV^{-2}, or 10^{-4} GeV^{-1} depending on the mass dimension of the theory. In models that contain vector dark matter, the ILC may be able to probe even weaker couplings in the case of low dark matter mass.

To compare with astrophysical bounds, we found that the ILC reach is strongly dependent on the exact dark matter model. If we assume that dark matter is relatively heavy (> 100 GeV) and interacts with a standard model particle in proportion to its mass, then the ILC is uncompetitive. However, in the case that dark matter is relatively light (< 10 GeV) then the bounds from the ILC are competitive with astrophysical bounds in many models. In addition, if dark matter happens to only interact with the standard model leptons then the ILC offers a unique possibility to discover dark matter. For this reason, an ILC search is complementary to those done at the LHC thanks to the different initial state.

ACKNOWLEDGMENTS

We would especially like to thank Jenny List for many detailed discussions regarding the ILC analysis and Andrea De Simone for correcting typos in a previous version. The work has been supported by the Helmholtz Alliance ''Physics at the Terascale'', the DFG SFB/TR9 ''Computational Particle Physics'', and the DFB SFB/TR33 (''The Dark Universe''). H. K. D. would like to thank the Aspen Center for Physics where part of this work was completed.

APPENDIX A: CROSS SECTIONS FOR ANNIHILATION

We give the full cross sections for annihilation of a pair of dark matter particles with mass M_χ into a pair of

standard model fermions with mass m_f. To find the expansion coefficients in $\sigma v \approx a + bv^2$, we perform the nonrelativistic approximation $s \approx 4M_\chi^2 + M_\chi^2 v^2 + \frac{3}{4}M_\chi^2 v^4$ [35]. Note that in order to find the correct result for the v^2 term in σv, it is necessary to expand up to order v^4 because of the appearance of $\sqrt{s}$ in the cross section formulas.

The total cross section is then given as the sum of the cross sections over all allowed final state fermions. This set is restricted both by kinematics ($m_f \leq M_\chi$) and by the assumed model. The latter also determines whether the coupling G_f is universal or particle-dependent.

We define the mass ratio $\xi \equiv m_f/M_\chi$ and the velocities of both particles $\beta_X \equiv \sqrt{1 - 4m_X^2/s}$ to compactify the following expressions.

Some of our effective operators have been analyzed before, for example Refs. [38,39], and we agree with the respective results for the annihilation cross sections.

1. Scalar WIMP

$$\sigma_{\mathrm{Sc}}^{\mathrm{SS}} = \frac{G_f^2}{8\pi s}\frac{\beta_f}{\beta_\chi}(s - 4m_f^2), \tag{A1}$$

$$\sigma v \approx \frac{G_f^2}{4\pi}\sqrt{1-\xi^2}\left[(1-\xi^2) + \frac{v^2}{8}(5\xi^2 - 2)\right]. \tag{A2}$$

$$\sigma_{\mathrm{Ps}}^{\mathrm{SS}} = \frac{G_f^2}{8\pi}\frac{\beta_f}{\beta_\chi}, \tag{A3}$$

$$\sigma v \approx \frac{G_f^2}{4\pi}\left[\sqrt{1-\xi^2} + \frac{v^2}{8}\frac{3\xi^2 - 2}{\sqrt{1-\xi^2}}\right]. \tag{A4}$$

$$\sigma_{\mathrm{Vec}}^{\mathrm{SV}} = \frac{G_f^2}{12\pi}\beta_f\beta_\chi(s + 2m_f^2), \tag{A5}$$

$$\sigma v \approx \frac{G_f^2}{12\pi}[M_\chi^2 v^2\sqrt{1-\xi^2}(\xi^2 + 2)]. \tag{A6}$$

$$\sigma_{\mathrm{Ax}}^{\mathrm{SV}} = \frac{G_f^2}{12\pi}\beta_f\beta_\chi(s - 4m_f^2), \tag{A7}$$

$$\sigma v \approx \frac{G_f^2}{6\pi}[M_\chi^2 v^2(1-\xi^2)^{3/2}]. \tag{A8}$$

$$\sigma_{\mathrm{Ch}}^{\mathrm{SV}} = \frac{G_f^2}{24\pi}\beta_f\beta_\chi(s - m_f^2), \tag{A9}$$

$$\sigma v \approx \frac{G_f^2 M_\chi^2}{48\pi}v^2\sqrt{1-\xi^2}(4 - \xi^2). \tag{A10}$$

$$\sigma_{\mathrm{Sc/Ps}}^{\mathrm{SF}} = \frac{G_f^2}{48\pi s}\frac{\beta_f}{\beta_\chi}[2s(4m_f^2 - 2M_\chi^2 + 3M_\Omega^2 \mp 6m_f M_\Omega) - 8m_f^2(3(M_\Omega \mp m_f)^2 + M_\chi^2) + s^2], \tag{A11}$$

$$\sigma v \approx \frac{G_f^2}{4\pi}\sqrt{1-\xi^2}[(1-\xi^2)(\xi M_\chi \mp M_\Omega)^2 + \frac{v^2}{24}((15\xi^2 - 6)M_\Omega^2 \mp 6\xi(5\xi^2 - 2)M_\chi M_\Omega + (15\xi^4 - 4\xi^2 + 4)M_\chi^2)], \tag{A12}$$

$$\sigma_{\mathrm{Sc/Ps}}^{\mathrm{SFr}} = \frac{G_f^2}{2\pi s}\frac{\beta_f^3}{\beta_\chi}(m_f \mp M_\Omega)^2 \tag{A13}$$

$$\sigma v \approx \frac{G_f^2}{\pi}\sqrt{1-\xi^2}^3(\xi M_\chi \mp M_\Omega)^2\left[1 + \frac{v^2}{8}(5\xi^2 - 2)\right]. \tag{A14}$$

2. Fermion WIMP

$$\sigma_{\mathrm{Sc}}^{\mathrm{FS}} = \frac{G_f^2}{16\pi}\beta_f\beta_\chi(s - 4m_f^2), \tag{A15}$$

$$\sigma v \approx \frac{G_f^2}{8\pi}v^2 M_\chi^2(1-\xi^2)^{3/2}. \tag{A16}$$

$$\sigma_{\mathrm{Ps}}^{\mathrm{FS}} = \frac{G_f^2}{16\pi}\frac{\beta_f}{\beta_\chi}s, \tag{A17}$$

$$\sigma v \approx \frac{G_f^2 M_\chi^2}{2\pi}\left[\sqrt{1-\xi^2} + \frac{v^2}{8}\frac{\xi^2}{\sqrt{1-\xi^2}}\right]. \tag{A18}$$

$$\sigma_{\mathrm{Vec}}^{\mathrm{FV}} = \frac{G_f^2}{12\pi s}\frac{\beta_f}{\beta_\chi}(s + 2M_\chi^2)(s + 2m_f^2), \tag{A19}$$

$$\sigma v \approx \frac{G_f^2 M_\chi^2}{2\pi}\left[\sqrt{1-\xi^2}(2 + \xi^2) + v^2\frac{-4 + 2\xi^2 + 11\xi^4}{24\sqrt{1-\xi^2}}\right]. \tag{A20}$$

$$\sigma_{\mathrm{Ax}}^{\mathrm{FV}} = \frac{G_f^2}{12\pi s}\frac{\beta_f}{\beta_\chi}[s(s - 4(m_f^2 + M_\chi^2)) + 28m_f^2 M_\chi^2], \tag{A21}$$

$$\sigma v \approx \frac{G_f^2 M_\chi^2}{2\pi}\left[\sqrt{1-\xi^2}\xi^2 + v^2\frac{8 - 28\xi^2 + 23\xi^4}{24\sqrt{1-\xi^2}}\right]. \tag{A22}$$

$$\sigma_{\mathrm{Ch}}^{\mathrm{FV}} = \frac{G_f^2}{48\pi s}\frac{\beta_f}{\beta_\chi}(s(s - m_f^2 + M_\chi^2) + 4m_f^2M_\chi^2), \quad \text{(A23)}$$

$$\sigma v \approx \frac{G_f^2M_\chi^2}{8\pi}\left[\sqrt{1-\xi^2} + v^2\frac{(2-\xi^2+2\xi^4)}{24\sqrt{1-\xi^2}}\right]. \quad \text{(A24)}$$

$$\sigma_{\mathrm{Ch}}^{\mathrm{FVr}} = \frac{G_f^2}{24\pi s}\frac{\beta_f}{\beta_\chi}((s - 4M_\chi^2)(s - m_f^2) + 6m_f^2M_\chi^2), \quad \text{(A25)}$$

$$\sigma v \approx \frac{G_f^2M_\chi^2}{4\pi}\left[\xi^2\sqrt{1-\xi^2} + v^2\frac{16 - 32\xi^2 + 19\xi^4}{24\sqrt{1-\xi^2}}\right]. \quad \text{(A26)}$$

$$\sigma_{\mathrm{Sc/Ps}}^{\mathrm{FtS}} = \frac{G_f^2}{48\pi s}\frac{\beta_f}{\beta_\chi}(s(s - M_\chi^2) \mp 6m_fM_\chi s + m_f^2(16M_\chi^2 - s)), \quad \text{(A27)}$$

$$\sigma v \approx \frac{G_f^2M_\chi^2}{8\pi}(1\mp\xi)^2\left[\sqrt{1-\xi^2} + v^2\frac{2 \pm 16\xi + 17\xi^2}{24\sqrt{1-\xi^2}}\right]. \quad \text{(A28)}$$

$$\sigma_{\mathrm{Sc/Ps}}^{\mathrm{FtSr}} = \frac{G_f^2}{96\pi s}\frac{\beta_f}{\beta_\chi}(5s^2 + 80m_f^2M_\chi^2 - 2s(7m_f^2 + 7M_\chi^2 \mp 6m_fM_\chi)), \quad \text{(A29)}$$

$$\sigma v \approx \frac{G_f^2M_\chi^2}{8\pi}(1\pm\xi)^2\left[\sqrt{1-\xi^2} + v^2\frac{14 \mp 40\xi + 29\xi^2}{24\sqrt{1-\xi^2}}\right]. \quad \text{(A30)}$$

$$\sigma_{\mathrm{Vec/Ax}}^{\mathrm{FtV}} = \frac{G_f^2}{24\pi s}\frac{\beta_f}{\beta_\chi}(s(4s - 7M_\chi^2) \pm 6m_fM_\chi s - m_f^2(7s - 40M_\chi^2)), \quad \text{(A31)}$$

$$\sigma v \approx \frac{G_f^2M_\chi^2}{4\pi}\left[(3 \pm 2\xi + \xi^2)\sqrt{1-\xi^2} + v^2\frac{14 \mp 12\xi - 31\xi^2 \pm 18\xi^3 + 29\xi^4}{24\sqrt{1-\xi^2}}\right]. \quad \text{(A32)}$$

$$\sigma_{\mathrm{Vec/Ax}}^{\mathrm{FtVr}} = \frac{G_f^2}{12\pi s}\frac{\beta_f}{\beta_\chi}(7s^2 + 76m_f^2M_\chi^2 - 4s(4m_f^2 + 4M_\chi^2 \pm 3m_fM_\chi)), \quad \text{(A33)}$$

$$\sigma v \approx \frac{G_f^2M_\chi^2}{2\pi}\left[(2\mp\xi)^2\sqrt{1-\xi^2} + v^2\frac{32 \pm 24\xi - 64\xi^2 \mp 36\xi^3 + 47\xi^4}{24\sqrt{1-\xi^2}}\right]. \quad \text{(A34)}$$

$$\sigma_{\mathrm{Ch}}^{\mathrm{FtV}} = \frac{G_f^2}{48\pi s}\frac{\beta_f}{\beta_\chi}(4m_f^2M_\chi^2 + s(s - m_f^2 - M_\chi^2)), \quad \text{(A35)}$$

$$\sigma v \approx \frac{G_f^2M_\chi^2}{8\pi}\left[\sqrt{1-\xi^2} + v^2\frac{(2-\xi^2+2\xi^4)}{24\sqrt{1-\xi^2}}\right]. \quad \text{(A36)}$$

$$\sigma_{\mathrm{Ch}}^{\mathrm{FtVr}} = \frac{G_f^2}{24\pi s}\frac{\beta_f}{\beta_\chi}((s - 4M_\chi^2)(s - m_f^2) + 6m_f^2M_\chi^2), \quad \text{(A37)}$$

$$\sigma v \approx \frac{G_f^2M_\chi^2}{4\pi}\left[\xi^2\sqrt{1-\xi^2} + v^2\frac{16 - 32\xi^2 + 19\xi^4}{24\sqrt{1-\xi^2}}\right]. \quad \text{(A38)}$$

3. Vector WIMP

$$\sigma_{\mathrm{Sc}}^{\mathrm{VS}} = \frac{G_f^2}{288M_\chi^4\pi s}\frac{\beta_f}{\beta_\chi}(s - 4m_f^2)(12M_\chi^4 + s^2 - 4M_\chi^2 s), \quad \text{(A39)}$$

$$\sigma v \approx \frac{G_f^2}{12\pi}\sqrt{1-\xi^2}\left[(1-\xi^2) + \frac{v^2}{24}(2 + 7\xi^2)\right]. \quad \text{(A40)}$$

$$\sigma_{\mathrm{Ps}}^{\mathrm{VS}} = \frac{G_f^2}{288M_\chi^4\pi}\frac{\beta_f}{\beta_\chi}(12M_\chi^4 + s^2 - 4M_\chi^2 s), \quad \text{(A41)}$$

$$\sigma v \approx \frac{G_f^2}{12\pi}\sqrt{1-\xi^2}\left[1 + \frac{v^2}{24}\frac{2+\xi^2}{1-\xi^2}\right]. \quad \text{(A42)}$$

$$\sigma_{\mathrm{Vec}}^{\mathrm{VV}} = \frac{G_f^2}{432\pi M_\chi^4}\beta_f\beta_\chi(s + 2m_f^2)(s^2 + 20M_\chi^2 s + 12M_\chi^4), \quad \text{(A43)}$$

$$\sigma v \approx \frac{G_f^2}{4\pi}M_\chi^2v^2\sqrt{1-\xi^2}(\xi^2 + 2). \quad \text{(A44)}$$

$$\sigma_{\mathrm{Ax}}^{\mathrm{VV}} = \frac{G_f^2}{432\pi M_\chi^4}\beta_f\beta_\chi(s - 4m_f^2)(s^2 + 20M_\chi^2 s + 12M_\chi^4), \quad \text{(A45)}$$

$$\sigma v \approx \frac{G_f^2}{2\pi}M_\chi^2v^2(1-\xi^2)^{3/2}. \quad \text{(A46)}$$

$$\sigma^{\mathrm{VV\,Ch}} = \frac{G_f^2}{864\pi M_\chi^4}\beta_f\beta_\chi(s-m_f^2)(s^2+20M_\chi^2 s+12M_\chi^4), \tag{A47}$$

$$\sigma v \approx \frac{G_f^2}{16\pi}M_\chi^2 v^2\sqrt{1-\xi^2}(4-\xi^4). \tag{A48}$$

$$\begin{aligned}\sigma^{\mathrm{VF}}_{\mathrm{Vec/Ax}} = {}& \frac{G^2}{4320\pi M_\chi^4 s}\frac{\beta_f}{\beta_\chi}[8m_f^4(-174M_\chi^4+2M_\chi^2 s+s^2)+4M_\chi^2 s(s-20M_\Omega^2)+s^2(10M_\Omega^2+7s))\\ & -2m_f^2(680M_\chi^6+152M_\chi^4(5M_\Omega^2+s)+s(40M_\chi^6+2M_\chi^4(70M_\Omega^2-31s)\pm 240m_f^3 M_\Omega M_\chi^2(10M_\chi^2-s^2)\\ & \pm 120m_f M_\chi^2 M_\Omega s(M_\chi^2-s)+M_\chi^2(76s^2-40M_\Omega^2 s)+s^2(20M_\Omega^2+3s))],\end{aligned} \tag{A49}$$

$$\begin{aligned}\sigma v \approx {}& \frac{G^2}{36\pi}\sqrt{1-\xi^2}[(1-\xi^2)((5\xi^2+4)M_\chi^2\mp 6\xi M_\chi M_\Omega+5M_\Omega^2)+\frac{v^2}{24}(\mp 6\xi(19\xi^2+2)M_\chi M_\Omega+3(25\xi^2+6)M_\Omega^2\\ & +(83\xi^4+136\xi^2+156)M_\chi^2)].\end{aligned} \tag{A50}$$

$$\begin{aligned}\sigma^{\mathrm{VFr}}_{\mathrm{Vec/Ax}} = {}& \frac{G_f^2}{2160\pi M_\chi^4 s}\frac{\beta_f}{\beta_\chi}[s^4+22m_f^2M_\chi^2+13M_\chi^4-8s^2(8m_f^4+15M_\Omega^2(m_f^2+M_\chi^2)\pm 5m_f M_\Omega(4m_f^2+5M_\chi^2))\\ & -32m_f^2M_\chi^4(37m_f^2\pm 50m_f M_\Omega+70M_\chi^2+45M_\Omega^2)+2s^3(6m_f^2\pm 20m_f M_\Omega+16M_\chi^2+15M_\Omega^2)\\ & +8M_\chi^2 s(24m_f^4+15M_\Omega^2(4m_f^2+3M_\chi^2)\pm 50m_f M_\Omega(2m_f^2+M_\chi^2)+119m_f^2M_\chi^2+40M_\chi^4),\end{aligned} \tag{A51}$$

$$\begin{aligned}\sigma v \approx {}& \frac{G_f^2}{9\pi}\sqrt{1-\xi^2}[(1-\xi^2)(3M_\Omega^2\pm 2\xi M_\chi M_\Omega+(3\xi^2+4)M_\chi^2)+\frac{v^2}{24}(3(2+7\xi^2)M_\Omega^2\pm 6\xi(2+\xi^2)M_\chi M_\Omega\\ & +(16+30\xi^2+29\xi^4)M_\chi^2)].\end{aligned} \tag{A52}$$

APPENDIX B: CROSS SECTIONS FOR DIRECT DETECTION

We now give results for the dark matter-nucleon scattering cross section at zero momentum transfer, σ^0, for all defined benchmark models. In a universal scenario, the effective coupling is independent of the quark ($G_q = G$), whereas it grows proportionally to the quark mass in a Yukawa-like model ($G_q = Gm_q/m_e$). We use the following definitions:

$$\frac{f_p}{M_P} \equiv \sum_{q=u,d,s} f_q^p\frac{G_q}{m_q}+\frac{2}{27}\left(1-\sum_{q=u,d,s}f_q^p\right)\sum_{q=c,b,t}\frac{G_q}{m_q}, \tag{B1}$$

$$d_p \equiv \sum_{q=u,d,s} G_q\Delta_q^p, \tag{B2}$$

$$b_p \equiv 2G_u + G_d, \tag{B3}$$

$$\tilde{b}_p \equiv b_p M_\chi + 2G_u m_u + G_d m_d \tag{B4}$$

with the numerical values for f_q^p and Δ_q^p listed in Refs. [67,68]

$$f_u^p = 0.020 \pm 0.004, \tag{B5}$$

$$f_d^p = 0.026 \pm 0.005, \tag{B6}$$

$$f_s^p = 0.118 \pm 0.062, \tag{B7}$$

$$\Delta_u^p = -0.427 \pm 0.013, \tag{B8}$$

$$\Delta_d^p = 0.842 \pm 0.012, \tag{B9}$$

$$\Delta_s^p = -0.085 \pm 0.018. \tag{B10}$$

Further more we define the reduced mass of the WIMP proton system,

$$\mu \equiv \frac{M_\chi M_p}{M_\chi + M_p}. \tag{B11}$$

The cross sections can be evaluated in a nonrelativistic approximation for the WIMP and by using the quark proton form factors listed above. See e.g., Ref. [36]. If a model is not listed, its scattering cross section equals zero, e.g., for pseudoscalar interactions that always vanish in a nonrelativistic model. Again, we agree with the respective results in Refs. [38,39] for comparable operators.

Cross sections for real final state particles can easily be derived from the following list by setting the vector form

factors b_p and $\tilde{b}_p$ to zero and rescaling f_p and d_p by a factor of 2.

1. Scalar WIMP

$$\sigma^0_{\text{SS Sc}} = \frac{\mu^2}{4\pi M_\chi^2} f_p^2, \tag{B12}$$

$$\sigma^0_{\text{SV Vec}} = \frac{\mu^2}{\pi} b_p^2, \tag{B13}$$

$$\sigma^0_{\text{SF Sc}} = \frac{\mu^2}{4\pi}\left(+f_p + \frac{\tilde{b}_p}{M_\Omega}\right)^2, \tag{B14}$$

$$\sigma^0_{\text{SF Ps}} = \frac{\mu^2}{4\pi}\left(-f_p + \frac{\tilde{b}_p}{M_\Omega}\right)^2, \tag{B15}$$

$$\sigma^0_{\text{SV Chi}} = \frac{\mu^2}{4\pi} b_p^2. \tag{B16}$$

2. Fermion WIMP

$$\sigma^0_{\text{FS Sc}} = \frac{\mu^2}{\pi} f_p^2, \tag{B17}$$

$$\sigma^0_{\text{FV Vec}} = \frac{\mu^2}{\pi} b_p^2, \tag{B18}$$

$$\sigma^0_{\text{FV Ax}} = 3\frac{\mu^2}{\pi} d_p^2, \tag{B19}$$

$$\sigma^0_{\text{FV Chi}} = \frac{\mu^2}{16\pi} b_p^2, \tag{B20}$$

$$\sigma^0_{\text{FVr Chi}} = 3\frac{\mu^2}{\pi} d_p^2, \tag{B21}$$

$$\sigma^0_{\text{FtS Sc}} = \frac{\mu^2}{16\pi}(b_p + f_p)^2, \tag{B22}$$

$$\sigma^0_{\text{FtS Ps}} = \frac{\mu^2}{16\pi}(b_p - f_p)^2, \tag{B23}$$

$$\sigma^0_{\text{FtV Vec}} = \frac{\mu^2}{\pi}(1/2 \cdot b_p - f_p)^2, \tag{B24}$$

$$\sigma^0_{\text{FtV Ax}} = \frac{\mu^2}{\pi}(1/2 \cdot b_p + f_p)^2, \tag{B25}$$

$$\sigma^0_{\text{FtV Chi}} = \frac{\mu^2}{16\pi} b_p^2. \tag{B26}$$

3. Vector WIMP

$$\sigma^0_{\text{VS Sc}} = \frac{\mu^2}{4\pi M_\chi^2} f_p^2, \tag{B27}$$

$$\sigma^0_{\text{VF Vec}} = \frac{\mu^2}{4\pi}\left(-f_p + \frac{\tilde{b}_p}{M_\Omega}\right)^2, \tag{B28}$$

$$\sigma^0_{\text{VF Ax}} = \frac{\mu^2}{4\pi}\left(+f_p + \frac{\tilde{b}_p}{M_\Omega}\right)^2, \tag{B29}$$

$$\sigma^0_{\text{VF Chi}} = \frac{\mu^2}{4\pi} b_p^2, \tag{B30}$$

$$\sigma^0_{\text{VV Vec}} = \frac{\mu^2}{\pi} b_p^2. \tag{B31}$$

4. Photon loop

If the WIMP only couples to leptons, the WIMP-proton interaction can only happen at the loop level. In that case, a low energy photon that couples to a virtual lepton pair interacts with the whole proton. This only happens for models with s-channel vector bilinears $\bar{\psi}\gamma^\mu\psi$, i.e., models which include either a, b_p, or a, $\tilde{b}_p$, term in the low energy tree level cross section. Results can therefore be derived as follows:

$$\sigma_0^{\text{Loop}} = \frac{\alpha_{\text{em}}^2}{81\pi^2} F^2(q^2)\sigma_0^{\text{Tree}}|_{\text{reduced}}, \tag{B32}$$

where the reduced cross section has to be understood as the tree level cross section given above after setting $b_p, \tilde{b}_p = 1$ and $f_p, d_p = 0$. This ensures that we only take the vector interaction parts. If the tree level cross section includes a b_p term, the loop factor is given as

$$F(q^2) \equiv \sum_l G_l f(q^2, m_l). \tag{B33}$$

For $\tilde{b}_p$ terms, it reads

$$F(q^2) \equiv \sum_l (m_l + M_\chi) G_l f(q^2, m_l). \tag{B34}$$

In both cases, the loop function can be evaluated as

$$f(q^2, m) \equiv \frac{1}{q^2}[5q^2 + 12m^2 - 6(q^2 + 2m^2)\beta_q \text{arcoth}\beta_q - 3q^2 \ln m^2/\Lambda^2], \tag{B35}$$

$$\beta_q \equiv \sqrt{1 - 4m^2/q^2}. \tag{B36}$$

We follow the conservative assumption of a maximum scattering angle to find $q^2 = -4\mu^2 v^2$ with μ describing the reduced mass of the WIMP nucleus system and $v = 500$ km/s being the typical escape velocity of a

WIMP in a dark matter halo. Because of the new q-dependence of the cross section and the fact that the photon only couples to the protons inside the nucleus, the official XENON results have to be rescaled according to

$$\sigma^{\text{Loop}} = \sigma^{\text{Tree}}\left[\frac{F(\tilde{q}^2)}{F(q^2)}\cdot\frac{A}{Z}\right]^2, \tag{B37}$$

where $\tilde{q} = q(M_N = M_P)$ uses the reduced mass μ of the WIMP proton system instead. This weakens the cross section limits by about a factor of 10.

APPENDIX C: DIFFERENTIAL CROSS SECTION FOR $e^+e^- \to \chi\chi\gamma$

1. Abbreviations

We use the following abbreviations for the final cross section list in Table III: Polarization prefactors:

$$C_S \equiv 1 + P^+P^-, \qquad C_V \equiv 1 - P^+P^-,$$
$$C_L \equiv (1 - P^-)(1 + P^+), \qquad C_R \equiv (1 + P^-)(1 - P^+). \tag{C1}$$

Terms with combined couplings:

$$G_{X\pm Y} \equiv g_X^2 \pm g_Y^2, \qquad G_{XY} \equiv g_X g_Y. \tag{C2}$$

Relativistic velocities:

$$\beta \equiv \sqrt{1 - \frac{4M_\chi^2}{s}}, \qquad \hat{\beta} \equiv \sqrt{1 - \frac{4M_\chi^2}{s(1-x)}}. \tag{C3}$$

Kinematical functions:

$$F_{x\theta} \equiv \frac{\alpha}{\pi}\frac{(x-1)^2+1}{x\sin^2\theta}, \tag{C4}$$

$$V_{x\theta} \equiv \frac{x^2\cos(2\theta) + (3x-8)x + 8}{4((x-1)^2+1)}. \tag{C5}$$

We show terms that arise in the analytical evaluation of the differential photon cross section in $e^+e^- \to \chi\chi\gamma$ but not in the Weizsäcker-Williams approximation in (C6)–(C10). They all vanish in the soft-photon limit $x \to 0$.

$$A_{SF} = \frac{(1 - V_{x\theta})}{4M_\Omega^2}\frac{\hat{s}}{1-x}[(g_s + g_p)^4 C_R + (g_s - g_p)^4 C_L], \tag{C6}$$

$$A_{SFr} = \frac{\alpha}{8\pi}\frac{\hat{s}}{M_\Omega^2}\frac{x}{1-x}[(g_s + g_p)^4 C_R + (g_s - g_p)^4 C_L], \tag{C7}$$

$$A_{FtS} = \frac{(1 - V_{x\theta})}{4}\left[C_S(\hat{s} - 4M_\chi^2) + \frac{1}{1-x}C_S(2M_\chi^2 + \hat{s})\right], \tag{C8}$$

$$\begin{aligned}A_{VF} = {} & 20G_{lr}^2 C_S(1 - V_{x\theta})\frac{x}{1-x}(\hat{s}^2 + 4M_\chi^2\hat{s} - 8M_\chi^4) + \frac{(g_l^4 C_L + g_t^4 C_R)}{M_\Omega^2}\left[-\frac{1}{32}\frac{x^4\sin^2(2\theta)\hat{s}(3\hat{s}^2 + 26M_\chi^2\hat{s} - 32M_\chi^4)}{(x-1)^2((x-1)^2+1)}\right. \\ & + 6\frac{x}{((x-1)^2+1)}\hat{s}(\hat{s}^2 + 7M_\chi^2\hat{s} - 24M_\chi^4) - \frac{1}{4}(1 - V_{x\theta})(21\hat{s}^3 + 282M_\chi^2\hat{s}^2 - 1144M_\chi^4\hat{s} + 160M_\chi^6) \\ & + \frac{3}{2}\frac{(1 - V_{x\theta})}{(1-x)}\hat{s}(\hat{s}^2 - 28M_\chi^2\hat{s} + 16M_\chi^4) + \frac{1}{4}\frac{(1 - V_{x\theta})}{(1-x)^2}\hat{s}(7\hat{s}^2 - 126M_\chi^2\hat{s} + 32M_\chi^4) \\ & \left. + \frac{(1 - V_{x\theta})}{(1-x)^3}\hat{s}(\hat{s}^2 + 2M_\chi^2\hat{s} + 6M_\chi^4)\right],\end{aligned} \tag{C9}$$

$$\begin{aligned}A_{VFr} = {} & \frac{(g_l^4 C_L + g_r^4 C_R)}{M_\Omega^2}\left[-\frac{1}{32}\frac{x^4\sin^2(2\theta)}{(x-1)^2((x-1)^2+1)}\hat{s}(\hat{s}^2 + 32M_\chi^2\hat{s} - 24M_\chi^4) + 2\frac{x}{((x-1)^2+1)}\hat{s}(\hat{s}^2 + 12M_\chi^2\hat{s} + 56M_\chi^4)\right. \\ & - \frac{1}{4}(1 - V_{x\theta})(7\hat{s}^3 + 144M_\chi^2\hat{s}^2 - 168M_\chi^4\hat{s} + 1280M_\chi^6) + \frac{1}{2}\frac{(1 - V_{x\theta})}{(1-x)}\hat{s}(\hat{s}^2 - 48M_\chi^2\hat{s} + 56M_\chi^4) \\ & \left. + \frac{1}{4}\frac{(1 - V_{x\theta})}{(1-x)^2}\hat{s}(9\hat{s}^2 - 272M_\chi^2\hat{s} + 104M_\chi^4) + 2\frac{(1 - V_{x\theta})}{(1-x)^3}\hat{s}(\hat{s}^2 + 2M_\chi^2\hat{s} + 6M_\chi^4)\right].\end{aligned} \tag{C10}$$

[1] G. Bertone, D. Hooper, and J. Silk, Phys. Rep. **405**, 279 (2005).

[2] S. P. Martin, in *Perspectives on Supersymmetry II*, edited by G. L. Kane (World Scientific, Singapore, 2010), pp. 1–153.

[3] M. Drees, R. Godbole, and P. Roy, *Theory and Phenomenology of Sparticles: An Account of Four-Dimensional* N = 1 *Supersymmetry in High Energy Physics* (World Scientific, Hackensack, 2004), p. 555.

[4] T. Appelquist, H.-C. Cheng, and B. A. Dobrescu, Phys. Rev. D **64**, 035002 (2001).

[5] N. Arkani-Hamed, A. G. Cohen, and H. Georgi, Phys. Lett. B **513**, 232 (2001).

[6] H.-C. Cheng and I. Low, J. High Energy Phys. 09 (2003) 051.

[7] M. W. Goodman and E. Witten, Phys. Rev. D **31**, 3059 (1985).

[8] A. Bouquet, P. Salati, and J. Silk, Phys. Rev. D **40**, 3168 (1989).

[9] A. Birkedal, K. Matchev, and M. Perelstein, Phys. Rev. D **70**, 077701 (2004).

[10] P. Konar, K. Kong, K. T. Matchev, and M. Perelstein, New J. Phys. **11**, 105004 (2009).

[11] C. Bartels and J. List, *Model-independent WIMP searches at the ILC*, eConf C0705302, COS02 (2007).

[12] C. Bartels and J. List, in LCWS 2008 Chicago Conference Proceedings (unpublished).

[13] C. Bartels and J. List, Conference Proceeding LCWS10 Beijing (unpublished).

[14] C. Bartels, M. Berggren, and J. List, Eur. Phys. J. C **72**, 2213 (2012).

[15] N. Bernal, A. Goudelis, Y. Mambrini, and C. Munoz, J. Cosmol. Astropart. Phys. 01 (2009) 046.

[16] H. K. Dreiner, O. Kittel, and U. Langenfeld, Phys. Rev. D **74**, 115010 (2006).

[17] H. K. Dreiner, O. Kittel, and U. Langenfeld, Eur. Phys. J. C **54**, 277 (2008).

[18] Q.-H. Cao, C.-R. Chen, C. S. Li, and H. Zhang, J. High Energy Phys. 08 (2011) 018.

[19] Y. Bai, P. J. Fox, and R. Harnik, J. High Energy Phys. 12 (2010) 048.

[20] P. J. Fox, R. Harnik, J. Kopp, and Y. Tsai, Phys. Rev. D **85**, 056011 (2012).

[21] J. Goodman, M. Ibe, A. Rajaraman, W. Shepherd, T. M. P. Tait, and H.-B. Yu, Phys. Rev. D **82**, 116010 (2010).

[22] J. Goodman, M. Ibe, A. Rajaraman, W. Shepherd, T. M. P. Tait, and H.-B. Yu, Phys. Lett. B **695**, 185 (2011).

[23] M. Beltran, D. Hooper, E. W. Kolb, Z. A. C. Krusberg, and T. M. P. Tait, J. High Energy Phys. 09 (2010) 037.

[24] A. Rajaraman, W. Shepherd, T. M. P. Tait, and A. M. Wijangco, Phys. Rev. D **84**, 095013 (2011).

[25] Y. Bai and T. M. P. Tait, arXiv:1208.4361.

[26] K. Cheung, P.-Y. Tseng, Y.-L. S. Tsai, and T.-C. Yuan, J. Cosmol. Astropart. Phys. 05 (2012) 001.

[27] M. T. Frandsen, F. Kahlhoefer, A. Preston, S. Sarkar, and K. Schmidt-Hoberg, J. High Energy Phys. 07 (2012) 123.

[28] U. Haisch, F. Kahlhoefer, and J. Unwin, arXiv:1208.4605.

[29] J. March-Russell, J. Unwin, and S. M. West, J. High Energy Phys. 08 (2012) 029.

[30] Y. Mambrini and B. Zaldivar, J. Cosmol. Astropart. Phys. 10 (2011) 023.

[31] S. Chatrchyan *et al.* (CMS Collaboration), J. High Energy Phys. 09 (2012) 094.

[32] ATLAS Collaboration, CERN Report No. ATLAS-CONF-2012-084, 2012 (unpublished).

[33] P. J. Fox, R. Harnik, J. Kopp, and Y. Tsai, Phys. Rev. D **84**, 014028 (2011).

[34] A. Kurylov and M. Kamionkowski, Phys. Rev. D **69**, 063503 (2004).

[35] M. Beltran, D. Hooper, E. W. Kolb, and Z. C. Krusberg, Phys. Rev. D **80**, 043509 (2009).

[36] P. Agrawal, Z. Chacko, C. Kilic, and R. K. Mishra, arXiv:1003.1912.

[37] J. A. Conley, H. K. Dreiner, and P. Wienemann, Phys. Rev. D **83**, 055018 (2011).

[38] J.-M. Zheng, Z.-H. Yu, J.-W. Shao, X.-J. Bi, Z. Li, and H.-H. Zhang, Nucl. Phys. **B854**, 350 (2012).

[39] Z.-H. Yu, J.-M. Zheng, X.-J. Bi, Z. Li, D.-X. Yao, and H.-H. Zhang, Nucl. Phys. **B860**, 115 (2012).

[40] N. Haba, K. Kaneta, S. Matsumoto, and T. Nabeshima, Acta Phys. Pol. B **43**, 405 (2012).

[41] A. Denner, H. Eck, O. Hahn, and J. Kublbeck, Nucl. Phys. **B387**, 467 (1992).

[42] J. M. Cornwall, D. N. Levin, and G. Tiktopoulos, Phys. Rev. D **10**, 1145 (1974).

[43] E. Komatsu *et al.* (WMAP Collaboration), Astrophys. J. Suppl. Ser. **192**, 18 (2011).

[44] E. Aprile *et al.* (XENON100 Collaboration), Phys. Rev. Lett. **109**, 181301 (2012).

[45] O. Adriani *et al.* (PAMELA Collaboration), Nature (London) **458**, 607 (2009).

[46] T. S. Coleman and M. Roos, Phys. Rev. D **68**, 027702 (2003).

[47] J. Angle, E. Aprile, F. Arneodo, L. Baudis, A. Bernstein *et al.*, Phys. Rev. Lett. **101**, 091301 (2008).

[48] E. A. Baltz and J. Edsjo, Phys. Rev. D **59**, 023511 (1998).

[49] T. Delahaye, R. Lineros, F. Donato, N. Fornengo, J. Lavalle, P. Salati, and R. Taillet, Astron. Astrophys. **501**, 821 (2009).

[50] T. Delahaye, R. Lineros, F. Donato, N. Fornengo, and P. Salati, Phys. Rev. D **77**, 063527 (2008).

[51] M. Perelstein and B. Shakya, Phys. Rev. D **82**, 043505 (2010).

[52] J. N. Bahcall and R. M. Soneira, Astrophys. J. Suppl. Ser. **44**, 73 (1980).

[53] T. Sjostrand, S. Mrenna, and P. Z. Skands, Comput. Phys. Commun. **178**, 852 (2008).

[54] M. Cirelli and G. Giesen, arXiv:1301.7079.

[55] W. B. Atwood *et al.* (LAT Collaboration), Astrophys. J. **697**, 1071 (2009).

[56] M. Cirelli and P. Panci, Nucl. Phys. **B821**, 399 (2009).

[57] N. Bernal and S. Palomares-Ruiz, Nucl. Phys. **B857**, 380 (2012).

[58] P. Ciafaloni, M. Cirelli, D. Comelli, A. De Simone, A. Riotto, and A. Urbano, J. Cosmol. Astropart. Phys. 06 (2011) 018.

[59] R. Abbasi *et al.* (IceCube Collaboration), arXiv:1210.3557.

[60] R. Abbasi *et al.* (IceCube Collaboration), Phys. Rev. D **85**, 042002 (2012).
[61] C. Bartels, WIMP Search and a Cherenkov Detector Prototype for ILC Polarimetry, https://pubdb.desy.de/fulltext/getfulltext.php?lid=17403&fid=46030.
[62] N. Phinney, N. Toge, and N. Walker, arXiv:0712.2361.
[63] A. Pukhov, E. Boos, M. Dubinin, V. Edneral, V. Ilyin *et al.*, arXiv:hep-ph/9908288.
[64] T. Abe *et al.* (ILD Concept Group-Linear Collider Collaboration), arXiv:1006.3396.
[65] W. A. Rolke, A. M. Lopez, and J. Conrad, Nucl. Instrum. Methods Phys. Res., Sect. A **551**, 493 (2005).
[66] C. Helebrant, D. Kafer, and J. List, *Proceedings of 34th International Conference on High Energy Physics (ICHEP 2008), Philadelphia, Pennsylvania, 2008*, eConf C080730.
[67] J. R. Ellis, K. A. Olive, and C. Savage, Phys. Rev. D **77**, 065026 (2008).
[68] G. Belanger, F. Boudjema, A. Pukhov, and A. Semenov, Comput. Phys. Commun. **180**, 747 (2009).